Weak structure functions in ν_l-N and ν_l-A scattering with nonperturbative and higher order perturbative QCD effects

F. Zaidi,[1] H. Haider,[2,†] M. Sajjad Athar,[1,*] S. K. Singh,[1] and I. Ruiz Simo[3]

[1]*Department of Physics, Aligarh Muslim University, Aligarh—202002, India*
[2]*Fermi National Accelerator Laboratory, Batavia, Illinois 60510, USA*
[3]*Departamento de Física Atómica, Molecular y Nuclear, and Instituto de Física Teórica y Computacional Carlos I, Universidad de Granada, Granada 18071, Spain*

(Received 28 November 2019; accepted 24 January 2020; published 11 February 2020)

We study the effect of various perturbative and nonperturbative QCD corrections on the free nucleon structure functions $[F_{iN}^{WI}(x, Q^2); i = 1\text{–}3]$ and their implications in the determination of nuclear structure functions. The evaluation of the nucleon structure functions has been performed by using the MMHT 2014 parton distribution functions (PDFs) parametrization, and the target mass correction (TMC) and higher twist (HT) effects are incorporated following the works of Schienbein *et al.* and Dasgupta *et al.*, respectively. These nucleon structure functions are taken as input in the determination of nuclear structure functions. The numerical calculations for the $\nu_l/\bar{\nu}_l$-A deep inelastic scattering (DIS) process have been performed by incorporating the nuclear medium effects like Fermi motion, binding energy, nucleon correlations, mesonic contributions, shadowing, and antishadowing in several nuclear targets such as carbon, polystyrene scintillator, iron, and lead, which are being used in MINERνA, and in argon nuclei, which is relevant for the ArgoNeuT and DUNE experiments. The differential scattering cross sections $\frac{d^2\sigma_A^{WI}}{dxdy}$ and $(\frac{d\sigma_A^{WI}}{dx}/\frac{d\sigma_{CH}^{WI}}{dx})$ have also been studied in the kinematic region of the MINERνA experiment. The theoretical results are compared with the recent experimental data of MINERνA and the earlier data of the NuTeV, CCFR, CDHSW, and CHORUS Collaborations. Moreover, a comparative analysis of the present results for the ratio $(\frac{d\sigma_A^{WI}}{dx}/\frac{d\sigma_{CH}^{WI}}{dx})$, and the results from the Monte Carlo (MC) generator GENIE and other phenomenological models of Bodek and Yang, and Cloet *et al.*, has been performed in the context of the MINERνA experiment. The predictions have also been made for the $\bar{\nu}_l$-A cross section relevant for the MINERνA experiment.

DOI: 10.1103/PhysRevD.101.033001

I. INTRODUCTION

Physicists are making continuous efforts in both the theoretical as well as the experimental fields for a better understanding of the hadronic structure and parton dynamics of nucleons, in a wide range of energy (E) and momentum transfer squared (Q^2). The deep inelastic scattering process with large values of four-momentum transfer squared has been used for a long time to explore the partonic distribution in the nucleon. Therefore, several studies are available concerning the perturbative region of high Q^2; however, much emphasis has not been given to the nonperturbative region of low Q^2. In a recent theoretical work [1], we have emphasized the effects of perturbative and nonperturbative QCD corrections in the evaluation of electromagnetic nucleon and nuclear structure functions. In the present paper, we have extended our analysis to the weak sector by considering the QCD corrections in the charged-current (anti)neutrino-induced deep inelastic scattering (DIS) process off free nucleon and nuclear targets. This study is to understand the effects of nonperturbative corrections such as target mass correction (TMC) and higher twist (HT) effects, the perturbative evolution of parton densities, nuclear medium modifications, isoscalarity corrections, and the center-of-mass (CoM) energy cut on the weak nuclear structure functions. Using these nuclear structure functions, the scattering cross section has been determined. This study is relevant for the development of precision experiments in order to determine accurately the

*Corresponding author.
sajathar@gmail.com
†On leave from Aligarh Muslim University.

neutrino oscillation parameters, and for the determination of mass hierarchy in the neutrino sector, etc., besides the intrinsic interest of understanding nucleon dynamics in the nuclear medium. For example, the planned DUNE experiment at Fermilab [2,3] is expected to get more than a 50% contribution to the event rates from the intermediate region of DIS and resonance production processes from nuclear targets. The ArgoNeuT Collaboration [4] has also measured the inclusive $\nu_l/\bar{\nu}_l$-^{40}Ar scattering cross section in the low-energy mode.

The ongoing MINERνA experiment at Fermilab is using an intermediate-energy (anti)neutrino beam, with the average energy of ∼6 GeV, where significant events contribute from the DIS processes. MINERνA has measured the scattering cross sections on the different nuclear targets (^{12}C, CH, ^{56}Fe, and ^{208}Pb) in the energy region, where various reaction channels such as quasielastic scattering (QES), inelastic scattering (IES), and DIS contribute, and has reported the ratio of charged-current deep inelastic differential scattering cross sections—i.e., $\frac{d\sigma^{C}/dx}{d\sigma^{CH}/dx}$, $\frac{d\sigma^{Fe}/dx}{d\sigma^{CH}/dx}$, and $\frac{d\sigma^{Pb}/dx}{d\sigma^{CH}/dx}$ [5]. For the DIS, the results have been analyzed by applying a cut on the four-momentum transfer squared $Q^2 \geq 1$ GeV^2 and the CoM energy $W \geq 2$ GeV, for the neutrino-induced processes, and their analysis is going on for the antineutrino-induced channel. They have compared the observed results with the phenomenological models like those being used in the GENIE Monte Carlo (MC) neutrino event generator [6] and the Bodek-Yang modified phenomenological parametrization [7], as well as from the phenomenological study of Cloet *et al.* [8]. It may be observed from the MINERνA analysis [5] that there is a large variation (∼20%) when all three phenomenological studies are compared. Furthermore, it is important to point out that in the MC event generators, the DIS cross sections are extrapolated phenomenologically to the region of low Q^2 in order to obtain the neutrino event rates. In this region, there is a lack of agreement between the experimental results from MINERνA and the results obtained from the various phenomenological analyses.

Therefore, it is important to understand nuclear medium effects, especially in the low-Q^2 region (1–5 GeV^2) in order to reduce the systematics in the neutrino oscillation analysis, which contributes ∼25% uncertainty to the systematics. The DIS cross section is described in terms of the nucleon structure functions—for example, by using $F_{1N}(x, Q^2)$ and $F_{2N}(x, Q^2)$ in the case of electromagnetic interaction, while for the weak interaction there is one more structure function, $F_{3N}(x, Q^2)$, that arises due to the parity violation. In the kinematic region of $Q^2 \to \infty, \nu \to \infty$, such that $x = \frac{Q^2}{2M_N\nu} \to$ constant, the nucleon structure functions become the function of a dimensionless variable x only, and $F_{1N}(x)$ and $F_{2N}(x)$ satisfy the Callan-Gross relation [9]:

$$F_{2N}(x) = 2xF_{1N}(x). \tag{1}$$

It implies that the Callan-Gross relation enables us to express the ν_l-N scattering cross section, in the massless limit of the lepton, in terms of only two nucleon structure functions $F_{2N}(x)$ and $F_{3N}(x)$. Through the explicit evaluation of the nucleon structure functions, one may write them in terms of the parton distribution functions (PDFs) which provide information about the momentum distribution of partons within the nucleon. Presently, various phenomenological parametrizations are available for the free nucleon PDFs. The different phenomenological groups have also proposed the nuclear PDFs, which are not a simple combination of free proton and free neutron PDFs. In the phenomenological analyses, the general approach is that the nuclear PDFs are obtained using the charged lepton–nucleus scattering data, and the ratios of the structure functions—e.g., $\frac{F_{2A}}{F_{2A'}}$, $\frac{F_{2A}}{F_{2D}}$—are analyzed, where A, A' represent any two nuclei and D stands for the deuteron, to take into account the nuclear correction factor. While determining the nuclear correction factor, the information regarding nuclear modification is also utilized from the Drell-Yan cross section ratio like $\frac{\sigma^{DY}_{pA}}{\sigma^{DY}_{pD}}$, $\frac{\sigma^{DY}_{pA}}{\sigma^{DY}_{pA'}}$, where p stands for the proton beam. Furthermore, the information about the nuclear correction factor is also supplemented by high-energy reaction data from the experiments at LHC, RHIC, etc. This approach has been used by Hirai *et al.* [10], Eskola *et al.* [11], Bodek and Yang [7], de Florian and Sassot [12], and others. The same nuclear correction factor is taken for the weak DIS processes. For example, Bodek and Yang [7] have obtained the nuclear correction factors for carbon, iron, gold, and lead using the charged lepton DIS data and applied the same nuclear correction factor to calculate the weak structure functions $2xF^{WI}_{1A}(x, Q^2)$, $F^{WI}_{2A}(x, Q^2)$, and $xF^{WI}_{3A}(x, Q^2)$. De Florian *et al.* [12] have analyzed ν_l-A DIS data, the charged lepton–nucleus scattering data, and Drell-Yan data to determine the nuclear corrections due to the medium effects. Their [12] conclusion is that the same nuclear correction factor can describe the nuclear medium effect in $l^{\pm}$-A and ν_l-A DIS processes. In the other approach, nuclear PDFs are directly parametrized by analyzing the experimental data—i.e., without using nucleon PDFs or a nuclear correction factor. This approach has been recently used to get $F^{EM}_{2A}(x, Q^2)$, $F^{WI}_{2A}(x, Q^2)$, and $F^{WI}_{3A}(x, Q^2)$ by the nCTEQ [13,14] group, who have collectively analyzed the charged lepton-A DIS and DY p-A dilepton production datasets [13] to determine the nuclear correction factor in the electromagnetic sector, and have performed an independent analysis for the $\nu_l(\bar{\nu}_l)$-A DIS datasets [14]. It has been concluded by them that the nuclear medium effects in $F^{EM}_{2A}(x, Q^2)$ are different from $F^{WI}_{2A}(x, Q^2)$, especially in the region of low x. Thus, in this region there is a

disagreement between the observation of these two studies [12,13], especially at low x [15].

Theoretically, many models have been proposed to study these effects on the basis of nuclear binding, nuclear medium modification including short-range correlations in nuclei [16–43], pion excess in nuclei [18,20,24,38–40], multiquark clusters [41–43], dynamical rescaling [44,45], nuclear shadowing [46,47], etc. Despite these efforts, no comprehensive theoretical or phenomenological understanding of the nuclear modifications of the bound nucleon structure functions across the complete range of x and Q^2 consistent with the presently available experimental data exists [21–23,48]. To understand nuclear modifications, theoretically various studies are available concerning the nuclear medium effects in the electromagnetic sector [1,22,48,49], but there are mainly two groups—namely, the group of Kulagin and Petti [20,27,29,50] and that of Haider *et al.* [32,34,35,51,52], who have made a comparative study of the nuclear medium effects in the electromagnetic- and weak-interaction-induced processes [52].

As the nucleon structure functions are the basic inputs in the determination of nuclear structure functions and the scattering cross section, therefore, proper understanding of the nucleon structure functions as well as the parton dynamics becomes quite important. In the region of low and moderate Q^2, the perturbative and nonperturbative QCD corrections such as Q^2 evolution of parton distribution functions from leading-order to higher-order terms [next-to-leading order (NLO), next-to-next-to-leading order (NNLO),…], the effects of target mass correction due to the massive quarks' production (e.g., charm, bottom, top), and higher twist (twist-4, twist-6,…) because of the multiparton correlations, become important. These nonperturbative effects are specifically important in the kinematical region of high x and low Q^2, sensitive to some of the oscillation parameters, and therefore they are of considerable experimental interest to the long-baseline oscillation experiments.

In this work, we have evaluated the nucleon structure functions by using the MMHT PDFs parametrization [53] up to next-to-next-to-leading order (NNLO) in the four-flavor (u, d, s, and c) scheme following Refs. [54–56]. The nonperturbative higher-twist effect is incorporated by using the renormalon approach [57], and the target mass correction is included following the works of Schienbein *et al.* [58]. After taking into account the QCD corrections at the free nucleon level, we have studied the modifications in the nuclear structure functions due to the presence of nuclear medium effects such as Fermi motion, binding energy, and nucleon correlations. These effects are incorporated through the use of a spectral function of the nucleon in the nuclear medium [24,59]. The effect of mesonic contribution has been included, which is found to be significant in the low and intermediate regions of x [24]. We have also included the effect of shadowing and antishadowing corrections following the works of Kulagin and Petti [27]. Furthermore, we have discussed the effect of the CoM energy (W) cut on ν_l-A and $\bar{\nu}_l$-A scattering cross sections. This paper is organized as follows.

In the next section (Sec. II), we present the formalism in brief for (anti)neutrino-nucleon and (anti)neutrino-nucleus DIS processes. Then we discuss the method of obtaining nuclear structure functions with medium effects such as Fermi motion, binding energy, nucleon correlations, mesonic contribution, and shadowing. In Sec. III, numerical results are presented and discussed, and in the last section (Sec. IV), we summarize our findings.

II. FORMALISM

A. Deep inelastic scattering of (anti)neutrinos from nucleons

The basic reaction for the (anti)neutrino-induced charged-current deep inelastic scattering process on a free nucleon target is given by

$$\nu_l(k)/\bar{\nu}_l(k)+N(p)\to l^-(k')/l^+(k')+X(p'),\quad l=e,\mu, \tag{2}$$

where k and k' are the four-momenta of the incoming and outgoing leptons, while p and p' are the four-momenta of the target nucleon and the jet of hadrons produced in the final state, respectively. This process is mediated by the W boson ($W^{\pm}$) (depicted in Fig. 1), and the invariant matrix element corresponding to the above reaction is given by

$$-i\mathcal{M}=\frac{iG_F}{\sqrt{2}}l_\mu\left(\frac{M_W^2}{q^2-M_W^2}\right)\langle X|J^\mu|N\rangle. \tag{3}$$

G_F is the Fermi coupling constant, M_W is the mass of the W boson, and $q^2=(k-k')^2$ is the four-momentum transfer squared. l_μ is the leptonic current, and $\langle X|J^\mu|N\rangle$ is the hadronic current for the neutrino-induced reaction. The general expression of the double differential scattering cross section (DCX) for the massless lepton limit ($m_l\to 0$) corresponding to the reaction given in Eq. (2) in the laboratory frame is expressed as

$$\frac{d^2\sigma_N^{WI}}{dxdy}=\frac{yM_N}{\pi}\frac{E}{E'}\frac{|\mathbf{k}'|}{|\mathbf{k}|}\bar{\sum}\sum|\mathcal{M}|^2, \tag{4}$$

where $x=\frac{Q^2}{2M_N\nu}$ is the Bjorken scaling variable; $y=\frac{p.q}{p.k}(=\frac{\nu}{E}$ in the lab frame) is the inelasticity; $\nu=E-E'$ is the energy transfer; M_N is the nucleon mass; $E\,(E')$ is the energy of the incoming (outgoing) lepton; and $\bar{\sum}\sum|\mathcal{M}|^2$ is the invariant matrix element squared, which is given in terms of the leptonic ($L_{\mu\nu}^{WI}$) and hadronic ($W_N^{\mu\nu}$) tensors as

$$\bar{\sum}\sum|\mathcal{M}|^2=\frac{G_F^2}{2}\left(\frac{M_W^2}{Q^2+M_W^2}\right)^2L_{\mu\nu}^{WI}W_N^{\mu\nu}, \tag{5}$$

with $Q^2 = -q^2 \geq 0$. $L^{WI}_{\mu\nu}$ is given by

$$L^{WI}_{\mu\nu} = 8(k_\mu k'_\nu + k_\nu k'_\mu - k.k' g_{\mu\nu} \pm i\epsilon_{\mu\nu\rho\sigma} k^\rho k'^\sigma). \quad (6)$$

Here the antisymmetric term arises due to the contribution from the axial-vector components, with +ve sign for an antineutrino and −ve sign for a neutrino. The hadronic tensor $W^{\mu\nu}_N$ is written in terms of the weak structure functions $W^{WI}_{iN}(\nu, Q^2)(i = 1\text{–}3)$ as

$$W^{\mu\nu}_N = \left(\frac{q^\mu q^\nu}{q^2} - g^{\mu\nu}\right) W^{WI}_{1N}(\nu, Q^2) + \frac{W^{WI}_{2N}(\nu, Q^2)}{M_N^2}\left(p^\mu - \frac{p.q}{q^2}q^\mu\right)\left(p^\nu - \frac{p.q}{q^2}q^\nu\right) - \frac{i}{2M_N^2}\epsilon^{\mu\nu\rho\sigma} p_\rho q_\sigma W^{WI}_{3N}(\nu, Q^2). \quad (7)$$

The nucleon structure function $W^{WI}_{3N}(\nu, Q^2)$ arises due to the vector–axial vector interference part of the weak interaction and is responsible for the parity violation.

The weak nucleon structure functions $W^{WI}_{iN}(\nu, Q^2)$ $(i = 1, 2, 3)$ are generally redefined in terms of the dimensionless nucleon structure functions $F^{WI}_{iN}(x, Q^2)$ as

$$\left.\begin{aligned} M_N W^{WI}_{1N}(\nu, Q^2) &= F^{WI}_{1N}(x, Q^2) \\ \nu W^{WI}_{2N}(\nu, Q^2) &= F^{WI}_{2N}(x, Q^2) \\ \nu W^{WI}_{3N}(\nu, Q^2) &= F^{WI}_{3N}(x, Q^2) \end{aligned}\right\}. \quad (8)$$

In general, the dimensionless nucleon structure functions are in turn written in terms of the parton distribution functions as

$$\left.\begin{aligned} F^{WI}_2(x) &= \sum_i x[q_i(x) + \bar{q}_i(x)] \\ xF^{WI}_3(x) &= \sum_i x[q_i(x) - \bar{q}_i(x)] \end{aligned}\right\}. \quad (9)$$

In the above expressions, i runs for the different allowed flavors of quarks (antiquarks) able to couple directly to the $W^\pm$, the variable x is the momentum fraction carried by a quark (antiquark) of the nucleon's momentum, and $q_i(x)$ $[\bar{q}_i(x)]$ represents the probability density of finding a quark (antiquark) with a momentum fraction x. Using Eqs. (5), (6), (7), and (8) in Eq. (4), the differential scattering cross section is obtained as

$$\frac{d^2\sigma^{WI}_N}{dxdy} = \frac{G_F^2 M_N E}{\pi}\left(\frac{M_W^2}{M_W^2 + Q^2}\right)^2 \times \left[xy^2 F^{WI}_{1N}(x, Q^2) + \left(1 - y - \frac{M_N xy}{2E}\right) F^{WI}_{2N}(x, Q^2) \pm xy\left(1 - \frac{y}{2}\right) F^{WI}_{3N}(x, Q^2)\right]. \quad (10)$$

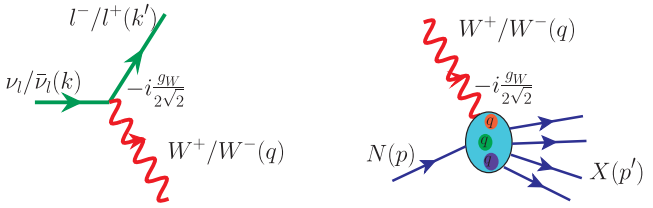

FIG. 1. Feynman representation for leptonic and hadronic vertices in the case of weak interaction.

We have evaluated the nucleon structure functions up to NNLO following the works of Vermaseren *et al.* [54] and Moch *et al.* [55,56]. These structure functions are expressed in terms of the convolution of a coefficient function $[C_{a,f};\ f = q, g$ and $a = 1\text{–}3)]$ with the density distribution of partons (f) inside the nucleon. For example, we may write $F^{WI}_{2N}(x)$ in terms of the coefficient function as

$$x^{-1}F^{WI}_{2N}(x) = \sum_{f=q,g} C_{2,f}(x) \otimes f(x), \quad (11)$$

with the perturbative expansion

$$C_{2,f}(x) = \sum_m \left(\frac{\alpha_s(Q^2)}{2\pi}\right)^m c^{(m)}_{2,f}, \quad (12)$$

where the superscript $m = 0, 1, 2, \ldots$ for $\mathrm{N}^{(m)}\mathrm{LO}$; $c^{(m)}_{2,f}(x)$ is the coefficient function for $F^{WI}_{2N}(x)$; $\alpha_s(Q^2)$ is the strong coupling constant; and the symbol $\otimes$ is the Mellin convolution, which turns into simple multiplication in the N space. To obtain the convolution of coefficient functions with parton density distribution, we use the following expression [60]:

$$C_{a,f}(x) \otimes f(x) = \int_x^1 C_{a,f}(y) f\left(\frac{x}{y}\right)\frac{dy}{y}. \quad (13)$$

The expression for the weak structure function $F^{WI}_{3N}(x)$ in terms of the coefficient function and the parton density distribution function is given by [56]

$$F^{WI}_{3N}(x) = \sum_{f=q,g} C_{3,f}(x) \otimes f(x) = C_{3,q}(x) \otimes q_v(x),$$

where $q_v(x)$ $[= f(x)]$ is the valence quark distribution for a $SU(3)/SU(4)$ symmetric sea and $C_{3,q}(x)$ is the coefficient function for $F^{WI}_{3N}(x)$.

In the kinematic region of low and moderate Q^2, both the higher-order perturbative and the nonperturbative $(\propto \frac{1}{Q^2})$ QCD effects come into play. For example, the nonperturbative target mass correction effect involves the powers of $\frac{1}{Q^2}$, and it is associated with the finite mass of the target nucleon. This effect is significant in the region of low Q^2

and high x, which is important in determining the valence quarks' distribution. The higher twist (HT) effect which is suppressed by $(\frac{1}{Q^2})^n, n = 1, 2, \ldots$, originates due to the interactions of struck quarks with the other quarks present in the surroundings via gluon exchange. This effect becomes small at low x and high Q^2. We have incorporated both the target mass correction and higher twist effects following Refs. [57,58], as well as performed the NNLO corrections in the evaluation of the nucleon structure functions. For the numerical calculations, we have used the MMHT nucleonic PDFs parametrization [53]. According to the operator product expansion [61,62], the weak nucleon structure functions with these nonperturbative effects can be mathematically expressed as

$$F_{iN}^{WI}(x, Q^2) = F_{iN}^{WI,\tau=2}(x, Q^2) + \frac{H_i^{\tau=4}(x, Q^2)}{Q^2}, \tag{14}$$

where the leading twist term ($\tau = 2$) incorporating the TMC effect obeys the Altarelli-Parisi evolution equations [63]. It is written in terms of PDFs and is responsible for the evolution of structure functions via perturbative QCD $\alpha_s(Q^2)$ corrections. The general expression of the twist-4 ($\tau = 4$) term that reflects the strength of multiparton correlations is given by [57]

$$H_i^{\tau=4}(x, Q^2) = A_2' \int_x^1 \frac{dz}{z} C_2^i(z) q\left(\frac{x}{z}, Q^2\right), \tag{15}$$

with $i = 1, 2, 3$. C_2^i is the coefficient function for twist 4, A_2' is the constant parameter, and $q(x/z, Q^2)$ is the quark density distribution.

We have incorporated the medium effects using a microscopic field theoretical approach. The effect of Fermi motion, binding energy, and nucleon correlations are included through the relativistic nucleon spectral function, which is obtained by using the Lehmann's representation for the relativistic nucleon propagator. We use the technique of nuclear many-body theory to calculate the dressed nucleon propagator in an interacting Fermi sea in the nuclear matter. To obtain the results for a finite nucleus, the local density approximation (LDA) is then applied. In the LDA, the Fermi momentum of an interacting nucleon is not a constant quantity but a function of the position coordinate (r) [59]. Since the nucleons bound inside a nucleus interact among themselves via the exchange of virtual mesons such as π, ρ, etc., a finite probability of the interaction of an intermediate vector boson with these mesons exists. We have also incorporated the mesonic contribution by using a many-body field theoretical approach similar to the case of bound nucleons [24]. Furthermore, the shadowing effect that dominates in the region of low x is taken into account, where the hadronization of intermediate vector bosons (W^+/W^-) creates quark-antiquark pairs that interact with the partons. The multiple scattering of quarks causes the destructive interference of amplitudes that leads to the phenomenon of shadowing which is incorporated in this paper, following the works of Kulagin and Petti [27]. In the next subsection, we have discussed the formalism adopted for the (anti)neutrino-nucleus scattering process.

B. Deep inelastic scattering of (anti)neutrinos from nuclei

In the case of DIS of (anti)neutrinos from nuclear targets, the expression of the differential cross section is given by

$$\frac{d^2\sigma_A^{WI}}{dxdy} = \frac{G_F^2 M_N y}{2\pi} \frac{E}{E'} \frac{|\mathbf{k}'|}{|\mathbf{k}|} \left(\frac{M_W^2}{M_W^2 + Q^2}\right)^2 L_{\mu\nu}^{WI} W_A^{\mu\nu}, \tag{16}$$

where $L_{\mu\nu}^{WI}$ is the weak leptonic tensor which has the same form as given in Eq. (6), while the nuclear hadronic tensor $W_A^{\mu\nu}$ is written in terms of the weak nuclear structure functions $W_{iA}^{WI}(\nu, Q^2)$ ($i = 1, 2, 3$) relevant in the case of $m_l \to 0$ as

$$\begin{aligned} W_A^{\mu\nu} = & \left(\frac{q^\mu q^\nu}{q^2} - g^{\mu\nu}\right) W_{1A}^{WI}(\nu, Q^2) \\ & + \frac{W_{2A}^{WI}(\nu, Q^2)}{M_A^2} \left(p_A^\mu - \frac{p_A.q}{q^2} q^\mu\right) \left(p_A^\nu - \frac{p_A.q}{q^2} q^\nu\right) \\ & - \frac{i}{2M_A^2} \epsilon^{\mu\nu\rho\sigma} p_{A\rho} q_\sigma W_{3A}^{WI}(\nu, Q^2). \end{aligned} \tag{17}$$

After contracting the leptonic tensor with the hadronic tensor and using the following relations between the nuclear structure functions $[W_{iA}^{WI}(\nu, Q^2)]$ and the dimensionless nuclear structure functions $[F_{iA}^{WI}(x, Q^2)]$:

$$M_A W_{1A}^{WI}(\nu, Q^2) = F_{1A}^{WI}(x, Q^2), \tag{18}$$

$$\nu W_{2A}^{WI}(\nu, Q^2) = F_{2A}^{WI}(x, Q^2), \tag{19}$$

$$\nu W_{3A}^{WI}(\nu, Q^2) = F_{3A}^{WI}(x, Q^2), \tag{20}$$

we obtain

$$\begin{aligned} \frac{d^2\sigma_A^{WI}}{dxdy} = & \frac{G_F^2 M_N E}{\pi} \left(\frac{M_W^2}{M_W^2 + Q^2}\right)^2 \left[xy^2 F_{1A}^{WI}(x, Q^2)\right. \\ & + \left(1 - y - \frac{M_N xy}{2E}\right) F_{2A}^{WI}(x, Q^2) \\ & \left. \pm xy\left(1 - \frac{y}{2}\right) F_{3A}^{WI}(x, Q^2)\right]. \end{aligned} \tag{21}$$

When the interaction takes place with a nucleon bound inside a nucleus, it gets influenced by the presence of other nucleons which are not stationary but are continuously

moving with a finite Fermi momentum. This motion of nucleons corresponds to the Fermi motion. These bound nucleons may also interact among themselves via strong interaction that is incorporated by the nucleon-nucleon correlations, and the binding energy for a given nucleus has also been ensured. Moreover, for a nonsymmetric nucleus such as iron, copper, tin, lead, etc., we have taken into account the different densities for the proton and the neutron. We have discussed these effects and present the formalism in the following subsection.

1. Fermi motion, binding energy, nucleon correlation, and isoscalarity effects

To calculate the scattering cross section for a neutrino interacting with a target nucleon in the nuclear medium, we express it in terms of the probability of interaction per unit area, which is defined as the probability of interaction per unit time of the particle (Γ) times the time spent in the interaction process (dt) over a differential area dS [1,49,52], i.e.,

$$d\sigma = \Gamma dt dS = \Gamma \frac{1}{v} d^3r = \Gamma \frac{E(\mathbf{k})}{|\mathbf{k}|} d^3r, \tag{22}$$

where $v(=\frac{|\mathbf{k}|}{E(\mathbf{k})})$ is the velocity of the particle and d^3r is the volume element. The probability of interaction per unit time (Γ) that the incoming neutrino will interact with the bound nucleons is related to the neutrino self-energy, which provides information about the total neutrino flux available at our disposal after the interaction:

$$\Gamma = -\frac{2m_l}{E(\mathbf{k})}\mathrm{Im}\Sigma \Rightarrow d\sigma = \frac{-2m_l}{|\mathbf{k}|}\mathrm{Im}\Sigma d^3r, \tag{23}$$

where $\mathrm{Im}\Sigma$ stands for the imaginary part of the neutrino self-energy that accounts for the depletion of the initial neutrinos flux out of the noninteracting channel, into the quasielastic or the inelastic channels. Thus, the imaginary part of the neutrino self-energy gives information about the total number of neutrinos that have participated in the interaction and give rise to the charged leptons. Therefore, the evaluation of the imaginary part of the neutrino self-energy is required to obtain the scattering cross section. Following the Feynman rules, we write the neutrino self-energy corresponding to the diagram shown in Fig. 2(a) as

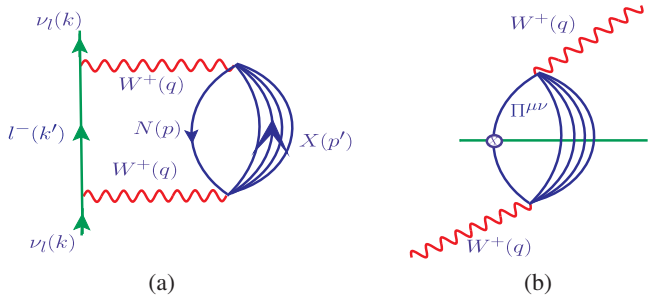

FIG. 2. Diagrammatic representation of the neutrino self-energy (left panel) and intermediate W boson self-energy (right panel).

$$\Sigma(k) = \frac{-iG_F}{\sqrt{2}}\int \frac{d^4k'}{(2\pi)^4}\frac{4L^{WI}_{\mu\nu}}{m_l}\frac{1}{(k'^2 - m_l^2 + i\epsilon)} \times \left(\frac{M_W}{Q^2 + M_W^2}\right)^2 \Pi^{\mu\nu}(q), \tag{24}$$

where we have used the properties of gamma matrices. The imaginary part of the neutrino self-energy may be obtained by using the Cutkosky rules [52] and is given by

$$\mathrm{Im}\Sigma(k) = \frac{G_F}{\sqrt{2}}\frac{4}{m_l}\int \frac{d^3k'}{(2\pi)^4}\frac{\pi}{E'(\mathbf{k}')}\theta(q^0) \times \left(\frac{M_W}{Q^2 + M_W^2}\right)^2 \mathrm{Im}[L^{WI}_{\mu\nu}\Pi^{\mu\nu}(q)]. \tag{25}$$

In the above expression, $\Pi^{\mu\nu}(q)$ is the W boson self-energy [depicted in Fig. 2(b)], which is defined in terms of the intermediate nucleon (G_l) and meson (D_j) propagators:

$$\Pi^{\mu\nu}(q) = \left(\frac{G_F M_W^2}{\sqrt{2}}\right) \times \int \frac{d^4p}{(2\pi)^4} G(p) \sum_X \sum_{s_p, s_l} \prod_{i=1}^{N} \int \frac{d^4p'_i}{(2\pi)^4} \prod_l G_l(p'_l) \prod_j D_j(p'_j) \times \langle X|J^\mu|N\rangle \langle X|J^\nu|N\rangle^* (2\pi)^4 \delta^4\left(p + q - \sum_{i=1}^{N} p'_i\right), \tag{26}$$

where s_p is the spin of the nucleon; s_l is the spin of the fermions in X; $\langle X|J^\mu|N\rangle$ is the hadronic current for the initial-state nucleon to the final-state hadrons; the indices l and j stand for the fermions and the bosons, respectively, in the final hadronic state X; and $\delta^4(p + q - \sum_{i=1}^{N} p'_i)$ ensures the conservation of four-momentum at the vertex. $G(p)$ is the nucleon propagator inside the nuclear medium through which the information about the propagation of the nucleon from the initial state to the final state or vice versa is obtained. The relativistic nucleon propagator for a noninteracting Fermi sea is written in terms of the positive $[u(p)]$ and negative $[v(-p)]$ energy components as

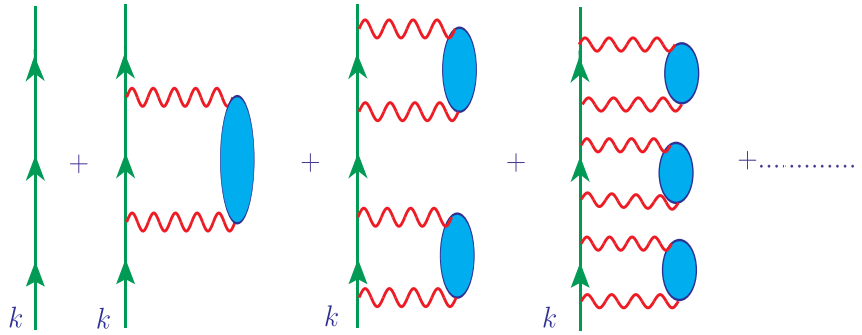

FIG. 3. Diagrammatic representation of nucleon self-energy in the nuclear medium.

$$G^0(p^0,\mathbf{p}) = \frac{M_N}{E_N(\mathbf{p})}\left\{\sum_r u_r(\mathbf{p})\bar{u}_r(\mathbf{p})\left[\frac{1-n(\mathbf{p})}{p^0 - E_N(\mathbf{p}) + i\epsilon} + \frac{n(\mathbf{p})}{p^0 - E_N(\mathbf{p}) - i\epsilon}\right] + \frac{\sum_r v_r(-\mathbf{p})\bar{v}_r(-\mathbf{p})}{p^0 + E_N(\mathbf{p}) - i\epsilon}\right\}.$$

The nucleon propagator retains the contribution only from the positive-energy components, because the negative energy components are much suppressed. Hence, we obtain

$$G^0(p^0,\mathbf{p}) = \frac{M_N}{E_N(\mathbf{p})}\sum_r u_r(\mathbf{p})\bar{u}_r(\mathbf{p}) \times \left[\frac{1-n(\mathbf{p})}{p^0 - E_N(\mathbf{p}) + i\epsilon} + \frac{n(\mathbf{p})}{p^0 - E_N(\mathbf{p}) - i\epsilon}\right].$$

In the above expression, the first term of the nucleon propagator within the square bracket contributes when the momentum of nucleon will be greater than or equal to the Fermi momentum, $|\mathbf{p}| \geq p_F$ (i.e., for the particles above the Fermi sea), while the second term within the square bracket contributes when the nucleon momentum will be less than the Fermi momentum, $|\mathbf{p}| < p_F$ (i.e., for the particles below the Fermi sea). This representation is known as the Lehmann representation [24]. Inside the Fermi sea, where nucleons interact with each other, the relativistic nucleon propagator $G(p)$ is obtained by using the perturbative expansion of Dyson series in terms of the nucleon self-energy (Σ^N) as

$$G(p) = G^0(p) + G^0(p)\Sigma^N(p)G^0(p) + G^0(p)\Sigma^N(p)G^0(p)\Sigma^N(p)G^0(p) + \cdots.$$

The nucleon self-energy (shown in Fig. 3) is evaluated by using the many-body field theoretical approach in terms of the spectral functions [24,59] and the dressed nucleon propagator $G(p)$ in an interacting Fermi sea is obtained as [59]

$$G(p) = \frac{M_N}{E_N(\mathbf{p})}\sum_r u_r(\mathbf{p})\bar{u}_r(\mathbf{p})\left[\int_{-\infty}^{\mu} d\omega \frac{S_h(\omega,\mathbf{p})}{p^0 - \omega - i\epsilon} + \int_{\mu}^{\infty} d\omega \frac{S_p(\omega,\mathbf{p})}{p^0 - \omega + i\epsilon}\right], \tag{27}$$

where $\mu = \epsilon_F + M_N$ is the chemical potential; $\omega = p^0 - M_N$ is the removal energy; and $S_h(\omega,\mathbf{p})$ and $S_p(\omega,\mathbf{p})$ are the hole and particle spectral functions, respectively. In the above expression, the term $S_h(\omega,\mathbf{p})d\omega$ is basically the joint probability of removing a nucleon from the ground state, and $S_p(\omega,\mathbf{p})d\omega$ is the joint probability of adding a nucleon to the ground state of a nucleus. Consequently, one may obtain the spectral function sum rule, which is given by

$$\int_{-\infty}^{\mu} S_h(\omega,\mathbf{p})d\omega + \int_{\mu}^{+\infty} S_p(\omega,\mathbf{p})d\omega = 1. \tag{28}$$

The expressions for the hole and particle spectral functions are given by [24,59]

$$S_h(p^0,\mathbf{p}) = \frac{1}{\pi}\frac{\frac{M_N}{E_N(\mathbf{p})}\mathrm{Im}\Sigma^N(p^0,\mathbf{p})}{(p^0 - E_N(\mathbf{p}) - \frac{M_N}{E_N(\mathbf{p})}\mathrm{Re}\Sigma^N(p^0,\mathbf{p}))^2 + (\frac{M_N}{E_N(\mathbf{p})}\mathrm{Im}\Sigma^N(p^0,\mathbf{p}))^2} \tag{29}$$

when $p^0 \leq \mu$, and by

$$S_p(p^0,\mathbf{p}) = -\frac{1}{\pi}\frac{\frac{M_N}{E_N(\mathbf{p})}\mathrm{Im}\Sigma^N(p^0,\mathbf{p})}{(p^0 - E_N(\mathbf{p}) - \frac{M_N}{E_N(\mathbf{p})}\mathrm{Re}\Sigma^N(p^0,\mathbf{p}))^2 + (\frac{M_N}{E_N(\mathbf{p})}\mathrm{Im}\Sigma^N(p^0,\mathbf{p}))^2} \tag{30}$$

when $p^0 > \mu$.

In the present study, we are considering the inclusive DIS process and are not looking at the final hadronic state; therefore, the interactions in the Fermi sea are taken into account through the hole spectral function S_h. Now, by using Eqs. (23) and (25), and performing the momentum space integration, the differential scattering cross section is obtained as

$$\frac{d\sigma_A^{WI}}{dxdy} = -\frac{G_F^2 M_N y}{2\pi}\frac{E}{E'}\frac{|\mathbf{k}'|}{|\mathbf{k}|}\left(\frac{M_W^2}{Q^2+M_W^2}\right)^2 \times \int \mathrm{Im}\left[L_{\mu\nu}^{WI}\Pi^{\mu\nu}(q)\right] d^3r. \tag{31}$$

On comparing Eqs. (16) and (31), it is found that the nuclear hadronic tensor $W_A^{\mu\nu}$ is related with the imaginary part of the W-boson self-energy $\mathrm{Im}\Pi^{\mu\nu}(q)$ as

$$W_A^{\mu\nu} = -\int \mathrm{Im}\Pi^{\mu\nu}(q) d^3r. \tag{32}$$

Using Eq. (27) and the expressions for the nucleon and meson propagators in Eq. (26), and finally substituting them in Eq. (32), we obtain the nuclear hadronic tensor $W_A^{\mu\nu}$ for an isospin symmetric nucleus in terms of the nucleonic hadronic tensor $W_N^{\mu\nu}$ convoluted with the hole spectral function (S_h) for a nucleon bound inside the nucleus:

$$W_A^{\mu\nu} = 4\int d^3r \int \frac{d^3p}{(2\pi)^3}\frac{M_N}{E_N(\mathbf{p})} \times \int_{-\infty}^{\mu} dp^0 S_h(p^0, \mathbf{p}, \rho(r)) W_N^{\mu\nu}(p,q), \tag{33}$$

where the factor of 4 is for spin-isospin of the nucleon, and $\rho(r)$ is the nuclear density. In general, the nuclear densities have various phenomenological parametrizations known in the literature as the harmonic oscillator (HO) density, the two-parameter Fermi density (2 pF), the modified harmonic oscillator (MHO) density, etc. The proton density distributions are obtained from the electron-nucleus scattering experiments, while the neutron densities are taken from the Hartee-Fock approach [64]. The density parameters c_1 and c_2 correspond to the charge density for the proton, or equivalently, the neutron matter density for the neutron. In the present model, for the numerical calculations, we have used the modified harmonic oscillator charge density

$$\rho(r) = \rho_0\left[1 + c_2\left(\frac{r}{c_1}\right)^2\right]e^{-\left(\frac{r}{c_1}\right)^2} \tag{34}$$

for the light nuclei, e.g., ^{12}C, and the two-parameter Fermi density

$$\rho(r) = \frac{\rho_0}{\left[1 + e^{\left(\frac{r-c_1}{c_2}\right)}\right]} \tag{35}$$

TABLE I. Different parameters used for the numerical calculations for various nuclei. For ^{12}C, we have used modified harmonic oscillator density (with the asterisk denoting that c_2 is dimensionless), and for ^{40}Ar, ^{56}Fe, and ^{208}Pb nuclei, two-parameter Fermi density has been used, where the superscripts n and p in density parameters ($c_i^{n,p}$; $i = 1, 2$) stand for the neutron and proton, respectively. Density parameters and the root-mean-square radius ($\langle r^2\rangle^{1/2}$) are given in units of femtometers. The kinetic energy of the nucleon per nucleus (T/A) and the binding energy of the nucleon per nucleus ($B.E./A$) for different nuclei are given in MeV.

	c_1		c_2				
Nucleus	c_1^n	c_1^p	c_2^n	c_2^p	$\langle r^2\rangle^{1/2}$	$B.E./A$	T/A
^{12}C	1.692	1.692	1.075*	1.075*	2.47	7.5	26.0
^{40}Ar	3.53	3.53	0.542	0.542	3.393	8.6	29.0
^{56}Fe	4.050	3.971	0.5935	0.5935	3.721	8.8	30.0
^{208}Pb	6.890	6.624	0.549	0.549	5.521	7.8	32.6

for the heavy nuclei, like ^{40}Ar, ^{56}Fe, and ^{208}Pb. In Eqs. (34) and (35), ρ_0 is the central density and c_1, c_2 are the density parameters [64,65] which are independently given for protons ($c_{1,2}^p$) and neutrons ($c_{1,2}^n$) in Table I along with the other parameters used in the numerical calculations. We ensure the normalization of the hole spectral function by obtaining the baryon number (A) of a given nucleus and the binding energy of the same nucleus:

$$4\int d^3r \int \frac{d^3p}{(2\pi)^3}\int_{-\infty}^{\mu} S_h(\omega, \mathbf{p}, \rho(r)) d\omega = A.$$

In the local density approximation, the spectral functions for the proton (Z) and neutron ($N = A - Z$) numbers in a nuclear target, which are functions of the local Fermi momenta $p_{F_{p,n}}(r) = [3\pi^2\rho_{p(n)}(r)]^{1/3}$, are normalized separately such that

$$2\int d^3r \int \frac{d^3p}{(2\pi)^3}\int_{-\infty}^{\mu_p} S_h^p(\omega, \mathbf{p}, \rho_p(r)) d\omega = Z,$$
$$2\int d^3r \int \frac{d^3p}{(2\pi)^3}\int_{-\infty}^{\mu_n} S_h^n(\omega, \mathbf{p}, \rho_n(r)) d\omega = N,$$

where the factor of 2 is due to the two possible projections of nucleon spin, μ_p (μ_n) is the chemical potential for the proton (neutron), and $S_h^p(\omega, \mathbf{p}, \rho_p(r))$ and $S_h^n(\omega, \mathbf{p}, \rho_n(r))$ are the hole spectral functions for the proton and neutron, respectively. The proton and neutron densities $\rho_p(r)$ and $\rho_n(r)$ are related to the nuclear density $\rho(r)$ as [49,52]

$$\rho_p(r) = \frac{Z}{A}\rho(r), \qquad \rho_n(r) = \frac{(A-Z)}{A}\rho(r).$$

Hence, for a nonisoscalar nuclear target, the nuclear hadronic tensor is written as

$$W_A^{\mu\nu} = 2\sum_{\tau=p,n}\int d^3r \int \frac{d^3p}{(2\pi)^3}\frac{M_N}{E_N(\mathbf{p})} \times \int_{-\infty}^{\mu_\tau} dp^0 S_h^\tau(p^0,\mathbf{p},\rho_\tau(r)) W_N^{\mu\nu}(p,q). \quad (36)$$

In this way, we have incorporated the effects of Fermi motion, Pauli blocking, and nucleon correlations through the hole spectral function.

From Eqs. (33) and (36), we have evaluated the nuclear structure functions by using the expressions of nucleon and nuclear hadronic tensors given in Eqs. (7) and (17), respectively, with the suitable choice of their components along the x, y, and z axes. The numerical calculations are performed in the laboratory frame, where the target nucleus is assumed to be at rest [$p_A=(p_A^0,\mathbf{p_A}=0)$], but the nucleons are moving with finite momentum [$p=(p^0,\mathbf{p}\neq 0)$]. These nucleons are thus off shell. If we choose the momentum transfer ($\mathbf{q}$) to be along the z axis—i.e., $q^\mu=(q^0,0,0,q^z)$—then the Bjorken variables for the nuclear target and the bound nucleons are defined as

$$x_A = \frac{Q^2}{2p_A\cdot q} = \frac{Q^2}{2M_A q^0} = \frac{Q^2}{2AM_N q^0},$$
$$x_N = \frac{Q^2}{2p\cdot q} = \frac{Q^2}{2(p^0q^0 - p^z q^z)}. \quad (37)$$

Hence, we have obtained the expressions of weak nuclear structure functions for the isoscalar and nonisoscalar nuclear targets by using Eqs. (33) and (36), respectively. The expression of $F_{1A,N}^{WI}(x_A,Q^2)$ is obtained by taking the xx component of the nucleon [Eq. (7)] and nuclear [Eq. (17)] hadronic tensors, which for an isoscalar nuclear target is given by

$$F_{1A,N}^{WI}(x_A,Q^2) = 4AM_N\int d^3r\int\frac{d^3p}{(2\pi)^3}\frac{M_N}{E_N(\mathbf{p})}\int_{-\infty}^{\mu} dp^0 S_h(p^0,\mathbf{p},\rho(r))\left[\frac{F_{1N}^{WI}(x_N,Q^2)}{M_N} + \left(\frac{p^x}{M_N}\right)^2\frac{F_{2N}^{WI}(x_N,Q^2)}{\nu_N}\right], \quad (38)$$

and for a nonisoscalar nuclear target is obtained as

$$F_{1A,N}^{WI}(x_A,Q^2) = 2\sum_{\tau=p,n} AM_N\int d^3r\int\frac{d^3p}{(2\pi)^3}\frac{M_N}{E_N(\mathbf{p})}\int_{-\infty}^{\mu_\tau} dp^0 S_h^\tau(p^0,\mathbf{p},\rho_\tau(r))\left[\frac{F_{1\tau}^{WI}(x_N,Q^2)}{M_N} + \left(\frac{p^x}{M_N}\right)^2\frac{F_{2\tau}^{WI}(x_N,Q^2)}{\nu_N}\right], \quad (39)$$

where $\nu_N = \frac{p\cdot q}{M_N} = \frac{p^0q^0 - p^zq^z}{M_N}$. We must point out that the evaluation of $F_{1A,N}^{WI}(x_A,Q^2)$ has been performed independently—i.e., without using the Callan-Gross relation at the nuclear level. Similarly, the zz component of the nucleon [Eq. (7)] and nuclear [Eq. (17)] hadronic tensors gives the expression of the dimensionless nuclear structure function $F_{2A,N}^{WI}(x_A,Q^2)$. For an isoscalar nuclear target, it is expressed as

$$F_{2A,N}^{WI}(x_A,Q^2) = 4\int d^3r\int\frac{d^3p}{(2\pi)^3}\frac{M_N}{E_N(\mathbf{p})}\int_{-\infty}^{\mu} dp^0 S_h(p^0,\mathbf{p},\rho(r)) \times\left[\frac{Q^2}{(q^z)^2}\left(\frac{|\mathbf{p}|^2-(p^z)^2}{2M_N^2}\right) + \frac{(p^0-p^z\gamma)^2}{M_N^2}\left(\frac{p^zQ^2}{(p^0-p^z\gamma)q^0q^z}+1\right)^2\right]\left(\frac{M_N}{p^0-p^z\gamma}\right)\times F_{2N}^{WI}(x_N,Q^2), \quad (40)$$

while for a nonisoscalar nuclear target it modifies to

$$F_{2A,N}^{WI}(x_A,Q^2) = 2\sum_{\tau=p,n}\int d^3r\int\frac{d^3p}{(2\pi)^3}\frac{M_N}{E_N(\mathbf{p})}\int_{-\infty}^{\mu_\tau} dp^0 S_h^\tau(p^0,\mathbf{p},\rho_\tau(r)) \times\left[\left(\frac{Q}{q^z}\right)^2\left(\frac{|\mathbf{p}|^2-(p^z)^2}{2M_N^2}\right) + \frac{(p^0-p^z\gamma)^2}{M_N^2}\left(\frac{p^zQ^2}{(p^0-p^z\gamma)q^0q^z}+1\right)^2\right]\left(\frac{M_N}{p^0-p^z\gamma}\right)\times F_{2\tau}^{WI}(x_N,Q^2), \quad (41)$$

with $\gamma=\frac{q^0}{q^z}$.

The expression of $F_{3A,N}^{WI}(x_A,Q^2)$ is obtained by choosing the xy component of the nucleon [Eq. (7)] and nuclear [Eq. (17)] hadronic tensors, which is given by

$$F_{3A,N}^{WI}(x_A,Q^2) = 4A\int d^3r\int\frac{d^3p}{(2\pi)^3}\frac{M_N}{E_N(\mathbf{p})}\int_{-\infty}^{\mu} dp^0 S_h(p^0,\mathbf{p},\rho(r))\times\frac{q^0}{q^z}\left(\frac{p^0q^z-p^zq^0}{p\cdot q}\right)F_{3N}^{WI}(x_N,Q^2) \quad (42)$$

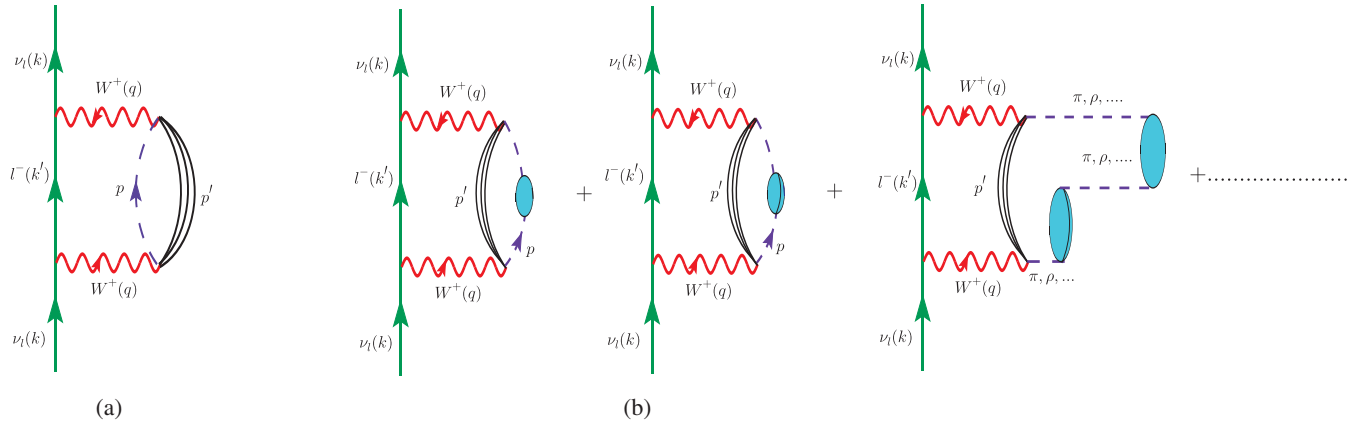

FIG. 4. Neutrino self-energy diagram accounting for neutrino-meson DIS. (a) The bound nucleon propagator is substituted with a meson (π or ρ) propagator of momentum p and a jet of hadrons X with momentum p'. (b) Cases including particle-hole (1p-1h), delta-hole (1Δ-1h), 1p1h-1Δ1h, etc., interactions.

for an isoscalar nuclear target. However, for a nonisoscalar nuclear target, we get

$$F_{3A,N}^{WI}(x_A, Q^2) = 2A \sum_{\tau=p,n} \int d^3r \int \frac{d^3p}{(2\pi)^3} \frac{M_N}{E_N(\mathbf{p})} \int_{-\infty}^{\mu_\tau} dp^0 S_h^\tau(p^0, \mathbf{p}, \rho_\tau(r)) \times \frac{q^0}{q^z} \left(\frac{p^0 q^z - p^z q^0}{p \cdot q} \right) F_{3\tau}^{WI}(x_N, Q^2). \quad (43)$$

The results obtained by using Eqs. (38), (40), (42) for isoscalar and Eqs. (39), (41), (43) for nonisoscalar nuclear targets are labeled as the results with the spectral function (SF) only.

2. Mesonic effect

In the case of (anti)neutrino-nucleus DIS processes, mesonic effects also contribute to the nuclear structure functions $F_{1A}^{WI}(x_A, Q^2)$ and $F_{2A}^{WI}(x, Q^2)$, which arises due to the interaction of bound nucleons among themselves via the exchange of virtual mesons such as π, ρ, etc. There is a reasonably good probability that an intermediate W boson may interact with a meson instead of a nucleon [24,27]. In order to include the contribution from the virtual mesons, we again evaluate the neutrino self-energy, for which a diagram is shown in Fig. 4, and write the meson hadronic tensor in the nuclear medium similar to the case of bound nucleons as [24]

$$W_{A,i}^{\mu\nu} = 3 \int d^3r \int \frac{d^4p}{(2\pi)^4} \theta(p_0)(-2) Im D_i(p) 2 m_i W_i^{\mu\nu}(p, q), \quad (44)$$

where $i = \pi$, ρ, the factor of 3 is due to the three charged states of pions (ρ mesons), and $D_i(p)$ is the dressed meson propagator. This expression is obtained by replacing the hole spectral function

$$-2\pi \frac{M_N}{E_N(\mathbf{p})} S_h(p_0, \mathbf{p}) W_N^{\mu\nu}(p, q)$$

in Eq. (33) with the imaginary part of the meson propagator—i.e,

$$Im D_i(p) \theta(p_0) 2 W_i^{\mu\nu}(p, q).$$

This meson propagator does not correspond to the free mesons because a lepton (either electron or muon) cannot decay into another lepton, one pion with a debris of hadrons, but it corresponds to the mesons arising due to the nuclear medium effects by using a modified meson propagator. These mesons are arising in the nuclear medium through particle-hole (1p-1h), delta-hole (1Δ-1h), 1p1h-1Δ1h, 2p-2h, etc., interactions as depicted in Fig. 4. This effect is incorporated following the mean-field theoretical approach of Ref. [24]. The expression of the meson propagator $[D_i(p)]$ in the nuclear medium is given by

$$D_i(p) = [p_0{}^2 - \mathbf{p}^2 - m_i^2 - \Pi_i(p_0, \mathbf{p})]^{-1}, \quad (45)$$

with the mass of the meson m_i and the meson self-energy Π_i, which is explicitly written as

$$\Pi_\pi = \left(\frac{f^2}{m_\pi^2} \right) \frac{F_\pi^2(p) \mathbf{p}^2 \Pi^*(p)}{1 - (\frac{f^2}{m_\pi^2}) V_L'(p) \Pi^*(p)},$$
$$\Pi_\rho = \left(\frac{f^2}{m_\pi^2} \right) \frac{C_\rho F_\rho^2(p) \mathbf{p}^2 \Pi^*(p)}{1 - (\frac{f^2}{m_\pi^2}) V_T'(p) \Pi^*(p)}. \quad (46)$$

In the above expressions, the coupling constant $f = 1.01$, the free parameter $C_\rho = 3.94$, $V_L'(p)$ $[V_T'(p)]$ is the

longitudinal (transverse) part of the spin-isospin interaction which is responsible for the enhancement to the pion (ρ meson) structure function, and $\Pi^*(p)$ is the irreducible meson self-energy that contains the contribution of particle-hole and delta-hole excitations. The πNN and ρNN form factors—i.e., $F_\pi(p)$ and $F_\rho(p)$—used in Eq. (46) are given by

$$F_\pi(p) = \frac{(\Lambda_\pi^2 - m_\pi^2)}{(\Lambda_\pi^2 + |\mathbf{p}|^2)}, \qquad F_\rho(p) = \frac{(\Lambda_\rho^2 - m_\rho^2)}{(\Lambda_\rho^2 + |\mathbf{p}|^2)}, \tag{47}$$

with the parameter $\Lambda_\pi(\Lambda_\rho) = 1$ GeV. Since Eq. (44) has taken into account the mesonic contents of the nucleon, which are already incorporated in the sea contribution of the nucleon, in order to calculate the mesonic excess in the nuclear medium we have subtracted the meson contribution of the nucleon [24] such that

$$ImD_i(p) \to \delta ImD_i(p) \equiv ImD_i(p) - \rho \frac{\partial ImD_i(p)}{\partial \rho}\bigg|_{\rho=0}. \tag{48}$$

Now we have obtained the following expression for the mesonic hadronic tensor:

$$W^{\mu\nu}_{A,i} = 3\int d^3r \int \frac{d^4p}{(2\pi)^4}\theta(p_0)(-2)\delta ImD_i(p) 2m_i W^{\mu\nu}_i(p,q). \tag{49}$$

Using Eq. (49), the mesonic structure functions $F^{WI}_{1A,i}(x,Q^2)$ and $F^{WI}_{2A,i}(x,Q^2)$ are evaluated following the same analogy as adopted in the case of bound nucleons [24]. The expression for $F^{WI}_{1A,i}(x,Q^2)$ is given by

$$F^{WI}_{1A,i}(x,Q^2) = -6\times a \times AM_N \int d^3r \int \frac{d^4p}{(2\pi)^4}\theta(p^0)\delta ImD_i(p) 2m_i \left[\frac{F^{WI}_{1i}(x_i)}{m_i} + \frac{|\mathbf{p}|^2 - (p^z)^2}{2(p^0q^0 - p^zq^z)}\frac{F^{WI}_{2i}(x_i)}{m_i}\right], \tag{50}$$

and for $F^{WI}_{2A,i}(x,Q^2)$ we obtain

$$F^{WI}_{2A,i}(x,Q^2) = -6\times a \int d^3r \int \frac{d^4p}{(2\pi)^4}\theta(p^0)\delta ImD_i(p) 2m_i \times \left[\frac{Q^2}{(q^z)^2}\left(\frac{|\mathbf{p}|^2 - (p^z)^2}{2m_i^2}\right) + \frac{(p^0 - p^z\gamma)^2}{m_i^2}\left(\frac{p^zQ^2}{(p^0 - p^z\gamma)q^0q^z} + 1\right)^2\right]\left(\frac{m_i}{p^0 - p^z\gamma}\right)F^{WI}_{2i}(x_i), \tag{51}$$

where $x_i = \frac{Q^2}{-2p\cdot q}$, and $a = 1$ for the pion and $a = 2$ for the ρ meson [24]. Notice that the ρ meson has an extra factor of 2 compared to the pionic contribution because of the two transverse polarizations of the ρ meson [66].

In the literature, various groups like MRST98 [67], CTEQ5L [68], SMRS [69], GRV [70], etc., have proposed the quark and antiquark PDF parametrizations for pions. We have observed in our earlier work [1] that the choice of different pionic PDF parametrizations would not make much difference in the scattering cross section. For the present numerical calculations, the GRV pionic PDF parametrizations given by Gluck *et al.* [70] have been used, and the same PDFs are also taken for the ρ meson. The contribution from the pion cloud is found to be larger than the contribution from the ρ meson cloud; nevertheless, the ρ contribution is non-negligible, and both of them are positive in the whole range of x. It is important to mention that $F^{WI}_{3A}(x_A,Q^2)$ has no mesonic contribution, as it depends mainly on the valence quark distribution, and these average to zero when considering the three charge states of pions and ρ mesons. For details, please see Refs. [1,49,52].

3. Shadowing and antishadowing effects

The shadowing effect which contributes in the region of low $x(\leq 0.1)$, takes place as a result of the destructive interference of the amplitudes due to the multiple scattering of quarks arising due to the hadronization of $W^\pm/Z^0$ bosons and leads to a reduction in the nuclear structure functions. It arises when the coherence length is larger than the average distance between the nucleons bound inside the nucleus and the expected coherence time is $\tau_c \geq 2$ fm. However, the shadowing effect gets saturated if the coherence length becomes larger than the average nuclear radius, i.e., in the region of low x. Furthermore, in the region of $0.1 < x < 0.3$, the nuclear structure functions get enhanced due to the antishadowing effect, which is theoretically less understood. In the literature, several studies proposed that it may be associated with the constructive interference of scattering amplitudes resulting from the multiple scattering of quarks [27,29,71]. For the antishadowing effect, the coherence time is small for the long internucleon spacing in the nucleus corresponding to these values of x. Shadowing and antishadowing effects are found to be quantitatively different in electromagnetic- and weak-interaction-induced processes [52]. It is because the electromagnetic and weak

interactions take place through the interaction of photons and $W^{\pm}/Z^0$ bosons, respectively, with the target hadrons and the hadronization processes of photons and $W^{\pm}/Z^0$ bosons being different. Moreover, in the case of weak interaction, the additional contribution of axial current which is not present in the case of electromagnetic interaction may influence the behavior of weak nuclear structure functions, especially if pions also play a role in the hadronization process through PCAC. Furthermore, in this region of low x, sea quarks also play an important role, which could be different in the case of electromagnetic and weak processes. In the present numerical calculations, we have incorporated the shadowing effect following the works of Kulagin and Petti [27], who have used Glauber-Gribov multiple scattering theory. For example, to determine the nuclear structure function $F_{iA}^{WI}(x, Q^2)$ with the shadowing effect, we use [27]

$$F_{iA}^{WI,S}(x, Q^2) = \delta R(x, Q^2) \times F_{iN}^{WI}(x, Q^2), \quad (52)$$

where $F_{iA}^{WI,S}(x, Q^2); (i = 1\text{–}3)$ is the nuclear structure function with the shadowing effect and the factor $\delta R(x, Q^2)$ is given in Ref. [27].

Now, using the present formalism, we have presented the results for the weak structure functions and scattering cross sections for both the free nucleon and nuclear targets in the next section.

III. RESULTS AND DISCUSSION

We have performed the numerical calculations by considering the following cases:

(1) The nucleon structure functions are obtained using PDF parametrizations of Martin *et al.* [53].
(2) All the results are presented with the TMC effect.
(3) $F_{iN}^{WI}(x, Q^2), (i = 1\text{–}3)$ are obtained at NLO and NNLO.
(4) At NLO, the higher twist effect has been incorporated following the renormalon approach [57], and a comparison is made with the results obtained at NNLO.
(5) After taking into account the perturbative and nonperturbative QCD corrections in the evaluation of free nucleon structure functions, we have used them to calculate the nuclear structure functions. The expression for $F_{iA}^{WI}(x, Q^2)$, $(i = 1, 2)$ in the full model is given by

$$F_{iA}^{WI}(x, Q^2) = F_{iA,N}^{WI}(x, Q^2) + F_{iA,\pi}^{WI}(x, Q^2) + F_{iA,\rho}^{WI}(x, Q^2) + F_{iA}^{WI,S}(x, Q^2), \quad (53)$$

where $F_{iA,N}^{WI}(x, Q^2)$ is the structure function with the spectral functions given in Eq. (38) [(39)] and Eq. (40) [(41)] for $F_{1A,N}^{WI}(x, Q^2)$ and $F_{2A,N}^{WI}(x, Q^2)$, respectively, in the case of isoscalar (nonisoscalar) targets, which takes care of Fermi motion, binding energy, and nucleon correlations. The mesonic contributions are included using Eqs. (50) and (51) for $F_{1A,j}^{WI}(x, Q^2)$ and $F_{2A,j}^{WI}(x, Q^2)$ $(j = \pi, \rho)$, respectively, and for the shadowing effect $[F_{iA}^{WI,S}(x, Q^2)]$, Eq. (52) is used. $F_{3A}^{WI}(x, Q^2)$ has no mesonic contribution, and the expression is given by

$$F_{3A}^{WI}(x, Q^2) = F_{3A,N}^{WI}(x, Q^2) + F_{3A,shd}^{WI}(x, Q^2) \quad (54)$$

with the spectral function contribution $F_{3A,N}^{WI}(x, Q^2)$, using Eq. (42) [(43)] for the isoscalar (nonisoscalar) nuclear targets and the shadowing correction $F_{3A,shd}^{WI}(x, Q^2)$ using Eq. (52).
(6) The results are presented for ^{12}C, CH, ^{40}Ar, ^{56}Fe, and ^{208}Pb nuclear targets, which are being used in the present-generation experiments.

The results of the free nucleon structure functions are presented in Fig. 5, for $2xF_{1N}^{WI}(x, Q^2)$, $F_{2N}^{WI}(x, Q^2)$, and $F_{3N}^{WI}(x, Q^2)$ vs Q^2 at $x = 0.225$, 0.45, and 0.65 in the case of the neutrino-nucleon DIS process. We observe that due to the TMC effect, the nucleon structure functions are modified at low and moderate Q^2, especially in the region of high x. We find that at NLO, the modification in the structure functions due to the TMC effect is about 3% (16%) in $2xF_{1N}^{WI}(x, Q^2)$, <1% (5%) in $F_{2N}^{WI}(x, Q^2)$, and 5% (10%) in $F_{3N}^{WI}(x, Q^2)$ at $x = 0.225$ (0.45) and $Q^2 = 1.8$ GeV^2, which becomes 1% (8%), <1% (1%), and ~2% (3%) at $Q^2 = 5$ GeV^2. On the other hand, the effect of higher twist corrections in this kinematic region is very small in $F_{1N}^{WI}(x, Q^2)$ and $F_{2N}^{WI}(x, Q^2)$, unlike in the case of electromagnetic structure functions [1]. By contrast, the effect of higher twist in $F_{3N}^{WI}(x, Q^2)$ leads to a decrease of 15% at $x = 0.225$ and one of 5% at $x = 0.65$ for $Q^2 = 1.8$ GeV^2, and it becomes small with the increase of Q^2. We observe that the difference in the results of $F_{iN}^{WI}(x, Q^2)$ $(i = 1, 2)$ at NLO with the HT effect from the results at NNLO is <1%. However, in $F_{3N}^{WI}(x, Q^2)$ at $x=0.225$, this difference is about 8% for $Q^2=1.8\,\text{GeV}^2$, and it reduces to ~2% for $Q^2 = 5$ GeV^2. With the increase in x and Q^2, the effect becomes gradually smaller.

The effect of higher twist is further suppressed in the nuclear medium, which is similar to our observation made for the electromagnetic nuclear structure functions [1]. The results observed at NLO with higher twist are close to the results obtained at NNLO. Therefore, all the results are presented here at NNLO.

In Figs. 6, 7, and 8, the results are presented for the nuclear structure functions $2xF_{1A}^{WI}(x, Q^2)$, $F_{2A}^{WI}(x, Q^2)$, and $xF_{3A}^{WI}(x, Q^2)$, respectively, vs Q^2 for the different values of x. The numerical results obtained in the kinematic limit $Q^2 > 1$ GeV^2 without any cut on the CoM energy W are

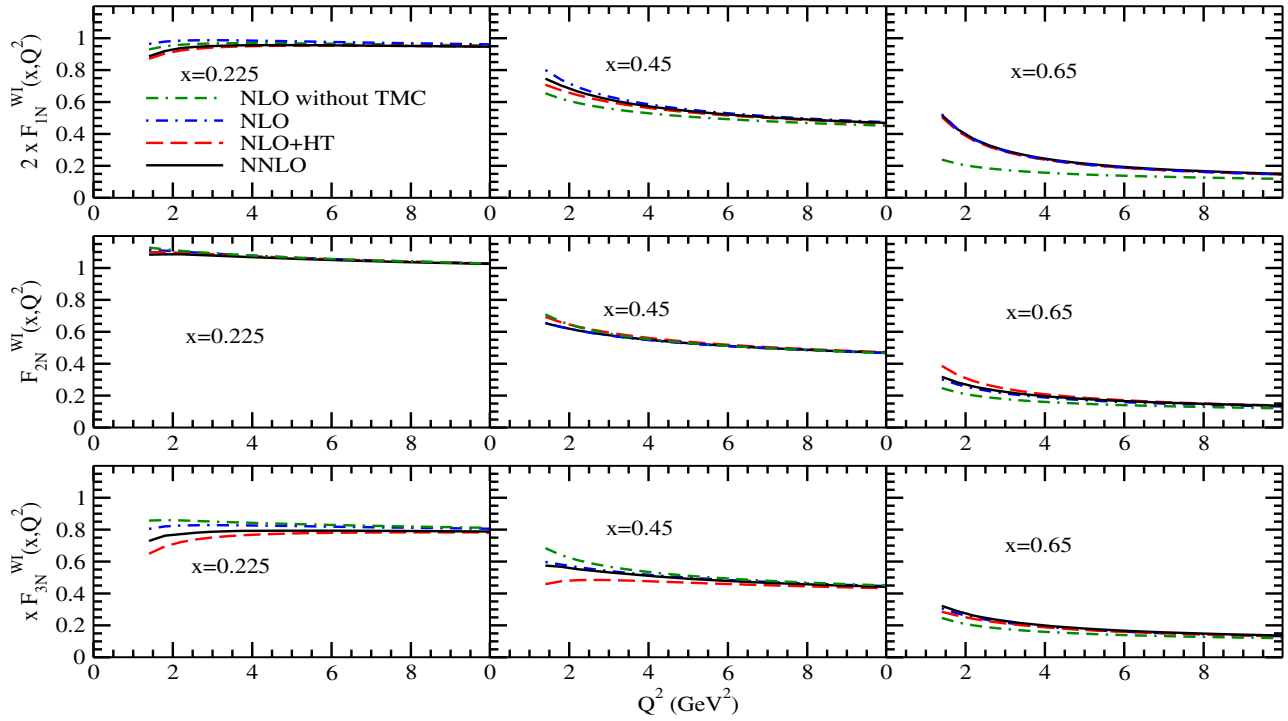

FIG. 5. $2xF_{1N}^{WI}(x,Q^2)$ (top panel), $F_{2N}^{WI}(x,Q^2)$ (middle panel), and $F_{3N}^{WI}(x,Q^2)$ (bottom panel) vs Q^2 at the different values of x for ν_l-N scattering. The results are obtained at NLO (i) without the TMC effect (double dash-dotted line), (ii) including the TMC effect without (dash-dotted line) and with (dashed line) the higher twist correction, and (iii) at NNLO with the TMC effect (solid line).

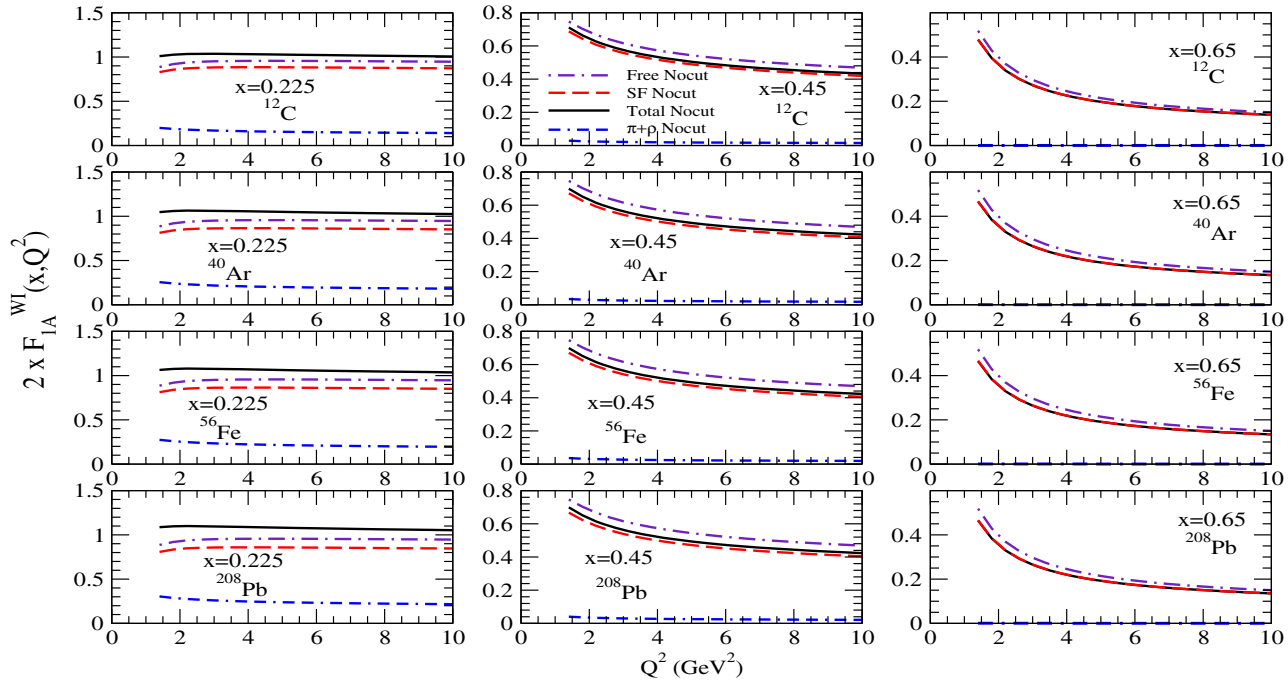

FIG. 6. Results for $2xF_{1A}^{WI}(x,Q^2)$ vs Q^2 are shown at different values of x for neutrino-induced DIS processes in ^{12}C, ^{40}Ar, ^{56}Fe, and ^{208}Pb. The results are obtained with the spectral function only (dashed line), with mesonic contributions only (double dash-dotted line) and with the full model (solid line) at NNLO, and they are compared with the results of the free nucleon case (dash-dotted line). All the nuclear targets are treated as isoscalar.

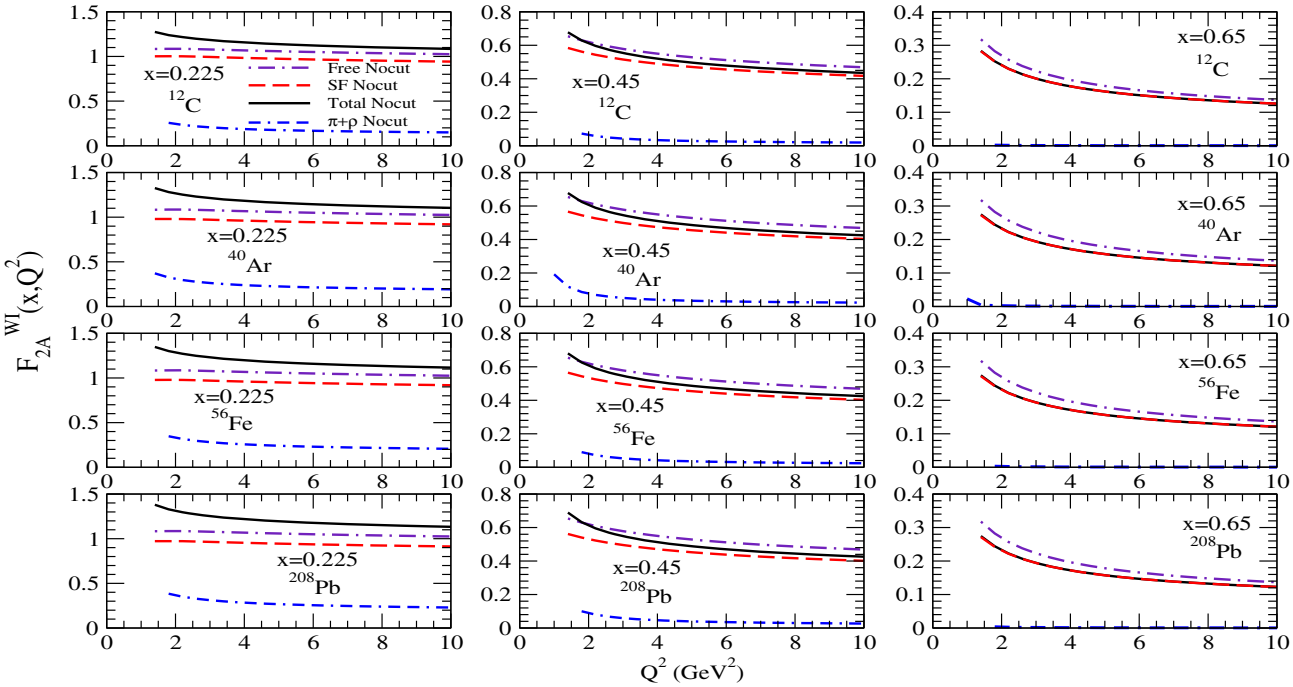

FIG. 7. $F_{2A}^{WI}(x, Q^2)$ vs Q^2. The lines in this figure have the same meaning as in Fig. 6.

labeled as "Nocut." The nuclear structure functions are shown for $1 < Q^2 \leq 10$ GeV^2 in carbon, argon, iron, and lead, which are treated as isoscalar nuclear targets and compared with the results obtained for a free nucleon target. From the figures, the different behavior of the nuclear medium effects in different regions of x and Q^2 can be clearly observed. For example, the results for the structure functions with spectral functions are suppressed from the results of the free nucleon target in the range of $x(< 0.7)$ and Q^2 considered here. Quantitatively, this reduction in carbon from the results of free nucleon structure functions for $Q^2 = 1.8$ GeV^2 is found to be about

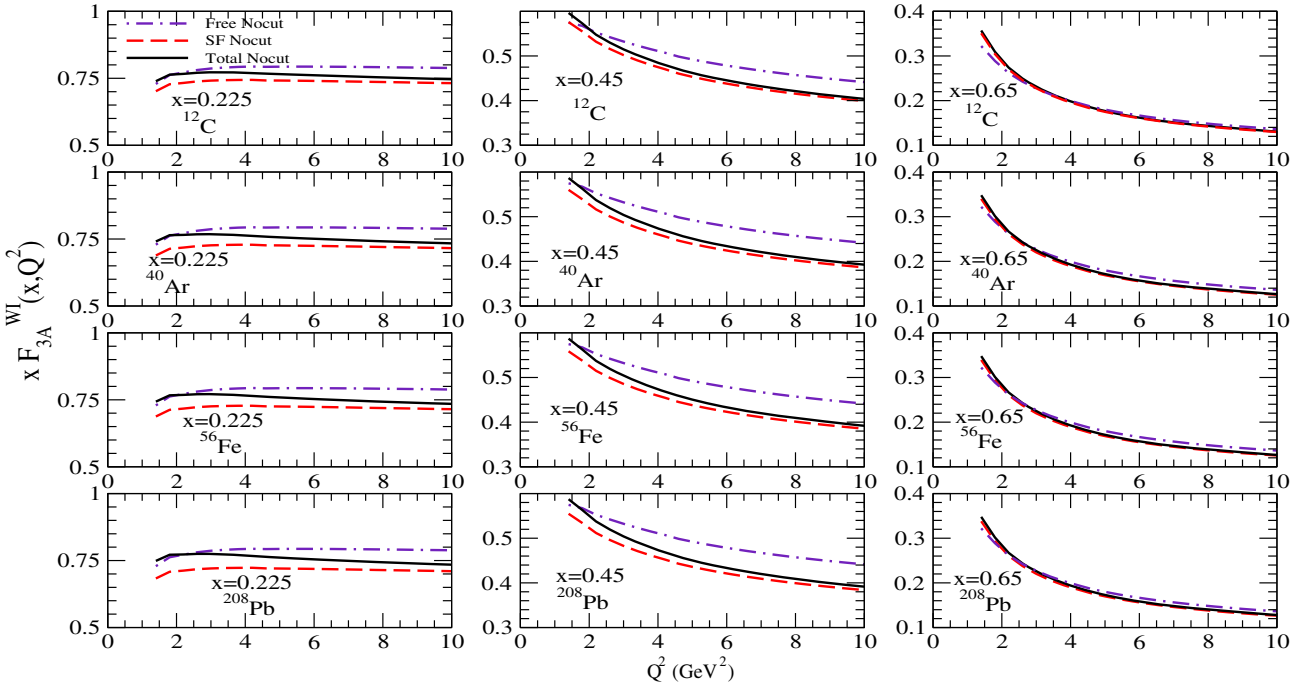

FIG. 8. $xF_{3A}^{WI}(x, Q^2)$ vs Q^2. The lines in this figure have the same meaning as in Fig. 6.

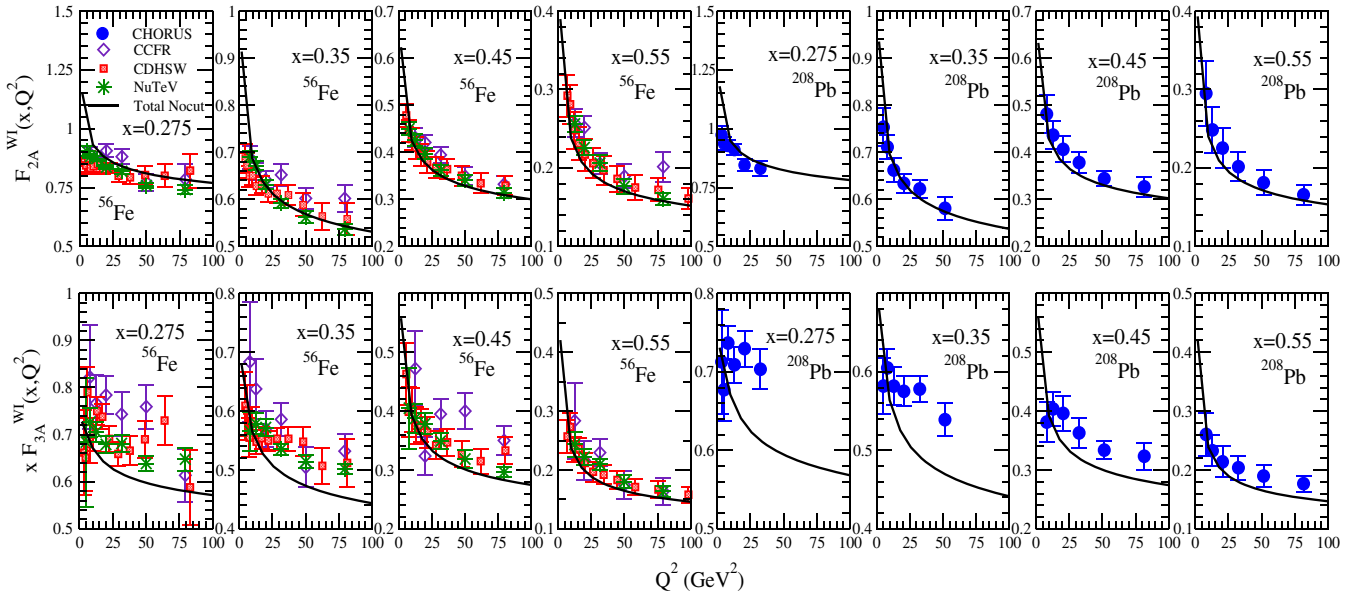

FIG. 9. Results for $F_{2A}^{\nu+\bar{\nu}}(x,Q^2)$ (top panel) and $xF_{3A}^{\nu+\bar{\nu}}(x,Q^2)$ (bottom panel) vs Q^2 are shown at different values of x in ^{56}Fe and ^{208}Pb. The results are obtained with the full model (solid line) at NNLO and are compared with the results of the available experimental data [72–75]. Both the nuclear targets are treated as isoscalar.

7%, 8%, and ∼5% at $x = 0.225$ in $2xF_{1A}^{WI}(x,Q^2)$, $F_{2A}^{WI}(x,Q^2)$, and $xF_{3A}^{WI}(x,Q^2)$, respectively, which becomes 9%, 11%, and 2% at $x = 0.45$. We have explicitly shown the mesonic contribution (double dash-dotted line), which is quite significant in the low and intermediate regions of $x(<0.6)$. The inclusion of mesonic effects gives an enhancement in the case of nuclear structure functions $F_{1A}^{WI}(x,Q^2)$ and $F_{2A}^{WI}(x,Q^2)$ for all values of $x < 0.6$ and becomes negligible for $x > 0.6$. The shadowing (antishadowing) effect that causes a reduction (enhancement) in the nuclear structure function for $x \leq 0.1$ $(0.1 < x < 0.3)$ is modulated by the mesonic contribution that works in its opposite (same) direction and results in an overall enhancement of the nuclear structure functions. Hence, the results obtained by including mesonic contributions, shadowing, and antishadowing effects in our full model are higher than the results with the spectral function only. The mesonic contribution does not contribute to $xF_{3A}^{WI}(x,Q^2)$. The difference between the results of the spectral function and the full model for $2xF_{1A}^{WI}(x,Q^2)$ is 20% at $x = 0.225$ and 3% at $x = 0.45$ for $Q^2 = 1.8$ GeV^2 in carbon. These nuclear effects are observed to be more pronounced for the heavy nuclear targets, such as in the case of argon, where it becomes 26% (4%); in lead, it becomes 31% (5%) at $x = 0.225$ $(x = 0.45)$ for $Q^2 = 1.8$ GeV^2. However, with the increase in Q^2, the mesonic contribution becomes small; for example, at $Q^2 = 5$ GeV^2, this difference is reduced to 16% in ^{12}C, 21% in ^{40}Ar, and 26% in ^{208}Pb at $x = 0.225$.

For the (anti)neutrino scattering cross sections and structure functions, high statistics measurements have been performed by the CCFR [72], CDHSW [73] and NuTeV [74] experiments in iron and by the CHORUS [75] Collaboration in lead nuclei. These experiments have been performed in a wide energy range—i.e., $20 \leq E_\nu \leq 350$ GeV—and the differential scattering cross sections have been measured. From these measurements, the nuclear structure functions are extracted. We study the nuclear modifications for the (anti)neutrino-induced processes in $F_{2A}^{\nu+\bar{\nu}}(x,Q^2)$ and $xF_{3A}^{\nu+\bar{\nu}}(x,Q^2)$ vs Q^2 in ^{56}Fe and ^{208}Pb nuclei by treating them as isoscalar nuclear targets. The results are presented in Fig. 9 at different values of x using the full model at NNLO and are compared with the available experimental data from the CCFR [72], CDHSW [73], NuTeV [74] and CHORUS [75] experiments. We find good agreement between the theoretical results for $F_{2A}^{\nu+\bar{\nu}}(x,Q^2)$ and reasonable agreement for $F_{3A}^{\nu+\bar{\nu}}(x,Q^2)$ with the experimental data.

We have also studied the nuclear modifications in the electromagnetic structure functions [1] and compared them with the weak structure functions for the free nucleon target, isoscalar nuclear targets, and nonisoscalar nuclear targets, and we present the results in Fig. 10 for the ratios $(\frac{5}{18})\frac{F_{1A}^{WI}(x,Q^2)}{F_{1A}^{EM}(x,Q^2)}$ (left panel) and $(\frac{5}{18})\frac{F_{2A}^{WI}(x,Q^2)}{F_{2A}^{EM}(x,Q^2)}$ (right panel) vs x at $Q^2 = 5$ and 20 GeV^2. The numerical results are shown at NNLO for carbon, iron, and lead with the full model and are compared with the results of free nucleons. It may be noticed from the figure that the ratio $R^{WI/EM}(x,Q^2)$ deviates from unity in the region of low x even for the free nucleon case. It implies a nonzero contribution from strange and charm quark distributions, which are found to be different in the case of electromagnetic and weak

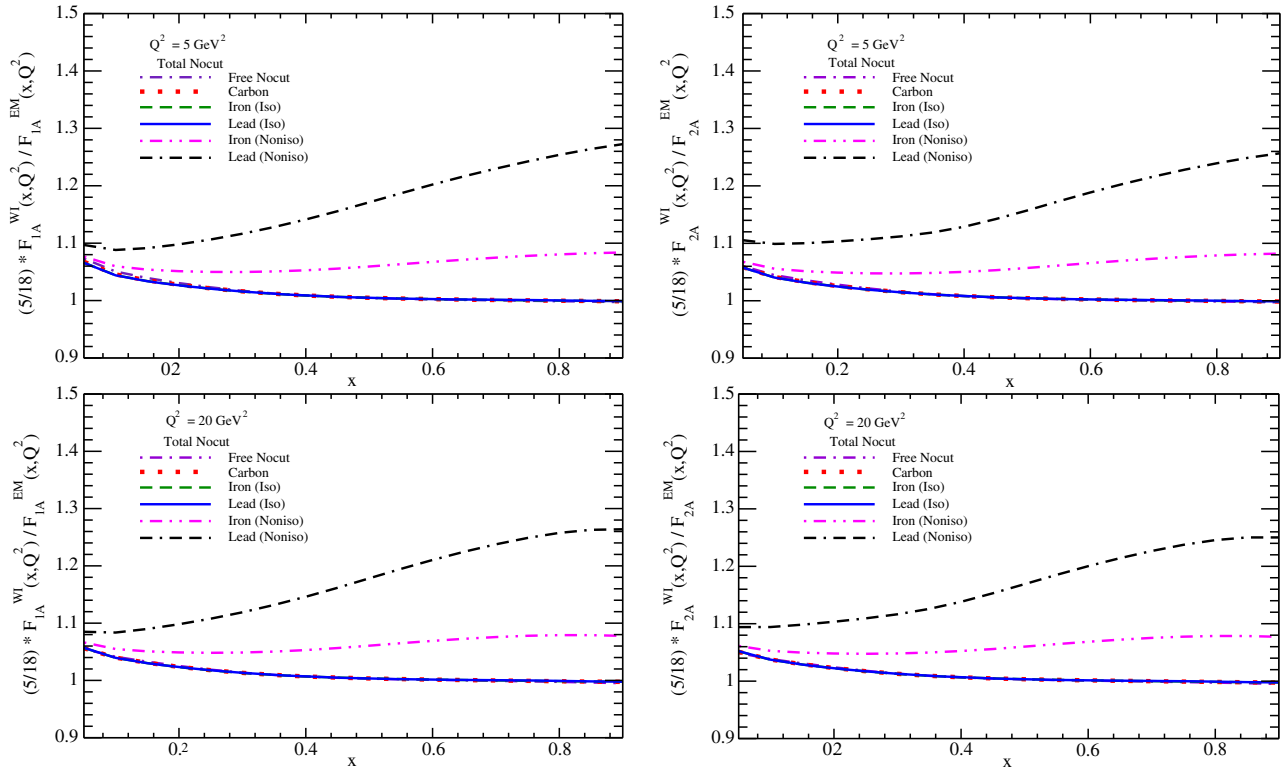

FIG. 10. The ratios $R^{WI/EM}(x,Q^2) = (\frac{5}{18})\frac{F_{iA}^{WI}(x,Q^2)}{F_{iA}^{EM}(x,Q^2)}$, $i = 1, 2$ vs x are shown at $Q^2 = 5$ GeV^2 (top panel) and 20 GeV^2 (bottom panel) in ^{12}C, ^{56}Fe and ^{208}Pb. The numerical results are obtained at NNLO using the full model and are compared with the free nucleon case.

structure functions. However, for $x \geq 0.4$, where the contributions of strange and charm quarks are almost negligible, the ratio approaches ~1. Furthermore, if one assumes $s = \bar{s}$ and $c = \bar{c}$, then in the region of small x, this ratio would be unity for an isoscalar nucleon target following the $(\frac{5}{18})$th sum rule. It may be seen that the difference between the ratio $R^{WI/EM}(x,Q^2)$ for the isoscalar nuclear targets and the free nucleon target is almost negligible. The evaluation is also done for the nonisoscalar nuclear targets ($N \gg Z$) like iron and lead. We must emphasize that in the present model, the spectral functions are normalized separately for the proton (Z) and neutron ($N = A - Z$) numbers in a nuclear target and to the number of nucleons for an isoscalar nuclear target [49]. The ratio $R^{WI/EM}(x,Q^2)$ shows a significant deviation for the nonisoscalar nuclear targets which increases with nonisoscalarity, i.e., $\delta = \frac{(A-Z)}{Z}$. This shows that the charm and strange quark distributions are significantly different in asymmetric heavy nuclei as compared to the free nucleons. It is important to notice that although some deviation is present in the entire range of x, it becomes more pronounced with the increase in x. For example, in iron (nonisoscalar), the deviation from the free nucleon case is 2% at $x = 0.2$, 5% at $x = 0.5$, and 8% at $x = 0.8$; while in lead (nonisoscalar), it is found to be ~7% at $x=0.2$, 16% at $x=0.5$, and 25% at $x=0.8$ at $Q^2 = 5$ GeV^2. This deviation also has some Q^2 dependence, and with the increase in Q^2, the deviation becomes smaller. From the figure, it may be observed that the isoscalarity corrections, significant in the region of large x, are different in $F_{1A}(x,Q^2)$ and $F_{2A}(x,Q^2)$, albeit the difference is small.

We have also presented the results for the ratios of nuclear structure functions, such as

$$\frac{F_{iA}^{WI}(x,Q^2)}{F_{iA'}^{WI}(x,Q^2)}, \quad (i=1,2,3; A=^{56}\text{Fe},^{208}\text{Pb}, \text{ and } A'=^{12}\text{C}) \text{ vs } x \tag{55}$$

at $Q^2 = 5$ GeV^2, in Fig. 11. The numerical results are shown with the full model at NNLO by treating iron and lead to be isoscalar as well as nonisoscalar nuclear targets. The following aspects are evident from the observation of Fig. 11:

(1) The deviation of the ratios $\frac{F_{i\text{Fe}}^{WI}(x,Q^2)}{F_{iC}^{WI}(x,Q^2)}$ and $\frac{F_{i\text{Pb}}^{WI}(x,Q^2)}{F_{iC}^{WI}(x,Q^2)}$ from unity in the entire range of x implies that nuclear medium effects are A dependent. From the figure, it may also be noticed that the ratio in lead is higher than the ratio in iron, which shows that medium effects become more pronounced with increased nuclear mass number. There is noticeable enhancement in the ratio obtained for the nonisoscalar case from the results obtained for the isoscalar nuclear

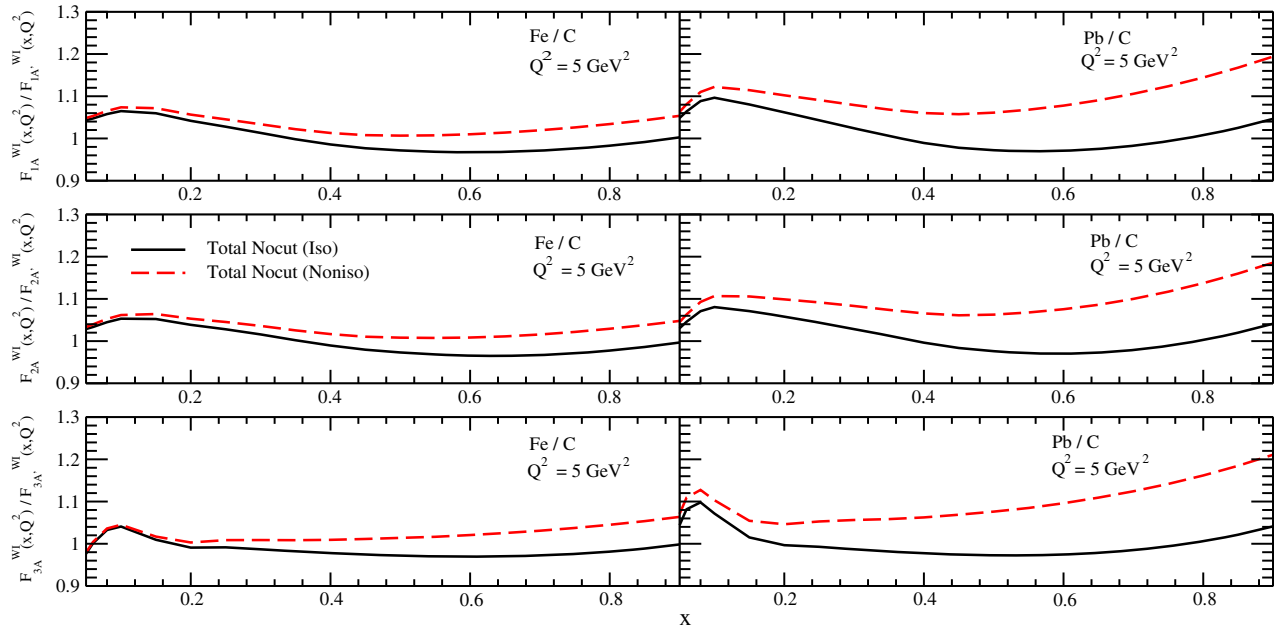

FIG. 11. $\frac{F_{iA}^{WI}(x,Q^2)}{F_{iA'}^{WI}(x,Q^2)}$, ($i = 1$–$3$; $A = {}^{56}$Fe, ^{208}Pb; $A' = {}^{12}$C) vs x are shown at $Q^2 = 5$ GeV^2. The results are obtained using the full model at NNLO by treating ^{56}Fe and ^{208}Pb as isoscalar (solid line) as well as nonisoscalar (dashed line) nuclear targets.

targets, especially at high x. This implies that the nonisoscalarity effect increases with an increase in x as well as the mass number.

(2) It is important to notice that although the behavior of the ratio is qualitatively the same in $\frac{F_{iA}^{WI}(x,Q^2)}{F_{iA'}^{WI}(x,Q^2)}$, ($i = 1$–$3$), quantitatively it is different.

In the literature, the choice of a sharp kinematical cut on W and Q^2 required to separate the regions of nucleon resonances and DIS—i.e., regions of shallow inelastic scattering and deep inelastic scattering—is debatable. However, in some of the analysis, the kinematic region of $Q^2 > 1$ GeV^2 and $W > 2$ GeV is considered to be the region of safe DIS [5,76], and this has been taken into account in the analysis of the MINERνA experiment [5]. Therefore, to explore the transition region of nucleon resonances and DIS, we have also studied the effect of a CoM cut on the scattering cross section. In Figs. 12–15, we have presented the results with a CoM cut of 2 GeV ($W > 2$ GeV) and $Q^2 > 1$ GeV^2, which are labeled as "Wcut," and we have compared them with the corresponding "Nocut" results ($Q^2 > 1$ GeV^2 only), as well as with the available experimental data.

In Figs. 12 and 13, the results are shown for $\frac{1}{E}\frac{d^2\sigma_A^{WI}}{dxdy}$ vs y for ν_l-A ($A = {}^{56}$Fe, ^{208}Pb) (top panel) and $\bar{\nu}_l$-A ($A = {}^{56}$Fe, ^{208}Pb) (bottom panel) scattering processes at NNLO. The numerical results are obtained for a beam energy of 35 GeV at different values of x. In Fig. 12, the theoretical results are presented for the spectral function only (dashed line) and for the full model (solid line) without having any cut on the CoM energy in iron, and they are compared with the NuTeV experimental data [74]. It may be seen that due to the mesonic contribution, the results with the full model are higher than the results with the spectral function at $x = 0.225$; however, for $x \geq 0.45$, where the mesonic contribution is suppressed, the difference becomes small. For example, in ν_l-^{56}Fe ($\bar{\nu}_l$-^{56}Fe), this enhancement is found to be 24% (30%) at $x = 0.225$ and 6% (8%) at $x = 0.45$ for $y = 0.2$. Furthermore, we have compared these results with the phenomenological results of nCTEQnu [77] (evaluated by using ν_l-A scattering experimental data). One may notice that the present theoretical results differ from the results of nCTEQnu PDF parametrizations [77] in the region of low x and y, while at high x and y they are in good agreement. In the inset of this figure, the results obtained with the full model having no cut on W (solid line) are compared with the results obtained with a cut of $W > 2$ GeV (solid line with star). It is important to notice that the difference between these results becomes more pronounced with increasing in x, especially at low y. For example, at $y = 0.1$ ($y = 0.4$), there is a difference of 30% (7%) at $x = 0.225$ and one of 36% (3%) at $x = 0.45$ in the ν_l-^{56}Fe scattering process; while for $\bar{\nu}_l$-^{56}Fe, the difference is found to be 32% (13%) and 37% (8%), respectively, at $x = 0.225$ and $x = 0.45$. For higher values of y, the effect of the CoM energy cut is small. However, there is no experimental data in the region of low y to test these results.

In Fig. 13, we have presented the numerical results of the differential scattering cross section in ^{208}Pb for the neutrino- and antineutrino-induced processes and compared them with the experimental data of the CHORUS [75]

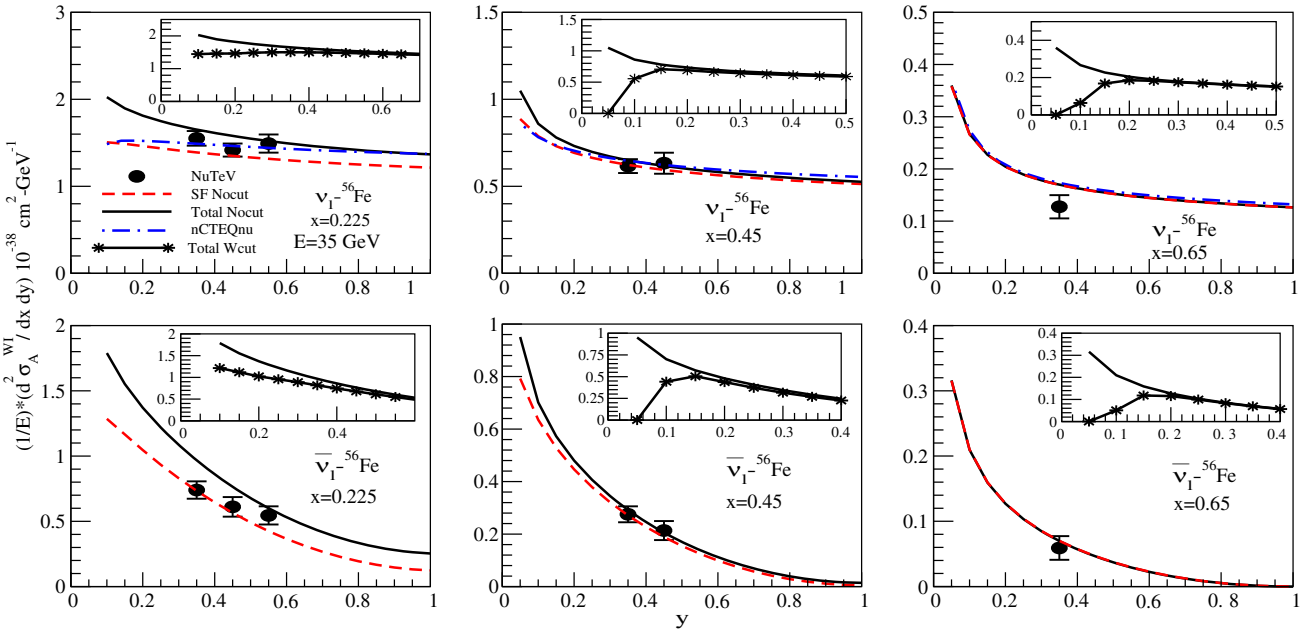

FIG. 12. $\frac{1}{E}\frac{d^2\sigma_A^{WI}}{dxdy}$ vs y are shown at different values of x for $E = 35$ GeV. The numerical results for ν_l-^{56}Fe DIS (top panel) and $\bar{\nu}_l$-^{56}Fe DIS (bottom panel) processes are obtained with the spectral function only (dashed line) and with the full model (solid line) at NNLO. In the inset, the results for the full model are compared with the corresponding results obtained with a kinematical cut of $W > 2$ GeV (solid line with star). Solid circles are the experimental data points of NuTeV [74]. The results for the ν_l-induced process obtained using the nuclear PDFs of nCTEQnu [77] (dash-dotted line) are also shown.

experiment, where a comparison of the theoretical results for ν_l-^{208}Pb scattering has also been made with the results of nCTEQnu [77] nuclear PDF parametrizations. We find that due to the A dependence, the nuclear medium effects are more pronounced in lead as compared to iron, and the effect of the CoM energy cut causes relatively larger suppression

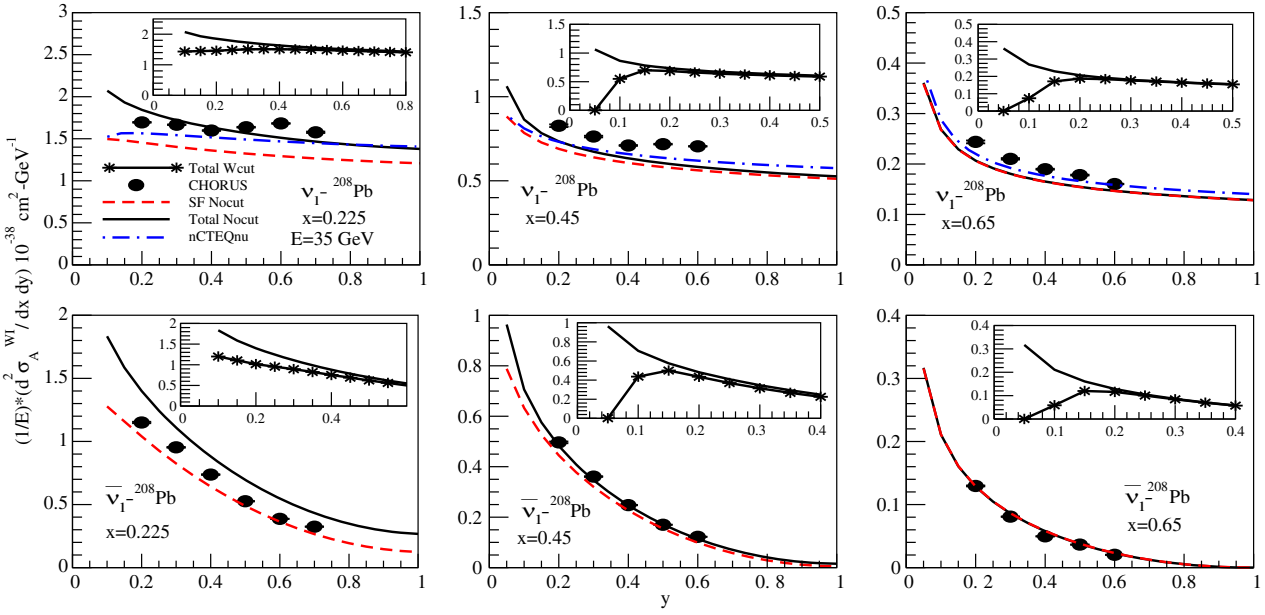

FIG. 13. $\frac{1}{E}\frac{d^2\sigma_A^{WI}}{dxdy}$ vs y are shown at different values of x for $E = 35$ GeV. The numerical results for ν_l-^{208}Pb DIS (top panel) and $\bar{\nu}_l$-^{208}Pb DIS (bottom panel) processes are obtained with the spectral function only (dashed line) and with the full model (solid line) at NNLO. In the inset, the results for the full model are compared with the corresponding results obtained with a kinematical cut of $W > 2$ GeV (solid line with star). Solid circles are the experimental data points of CHORUS [75]. The results for the ν_l-induced process obtained using the nuclear PDFs of nCTEQnu [77] (dash-dotted line) are also shown.

in the region of low x and y (≤ 0.4). For the numerical results presented in Figs. 12 and 13, the nuclear targets are treated as isoscalar.

The MINERνA experiment has used the NuMI neutrino beam at Fermilab for the cross section measurements in the low- and medium-energy modes that peak around neutrino energy of 3 GeV and 6 GeV, respectively. The low-energy neutrino broadband energy spectrum that peaks at ∼3 GeV extends up to 100 GeV; however, the neutrino flux drops steeply at high energies. The MINERνA Collaboration [5] has reported the ratio of flux integrated differential scattering cross sections in carbon, iron, and lead to the polystyrene scintillator (CH) vs x in the neutrino energy range of 5–50 GeV. We have chosen two neutrino beam energies viz. $E = 7$ GeV and 25 GeV, in a wide energy spectrum ($7 \leq E \leq 25$ GeV), in order to study the energy dependence of the nuclear medium effects. We have obtained $\frac{d\sigma_A^{WI}}{dx}$ by integrating Eq. (21) over y in the limits 0 and 1 and present the theoretical results for the ratio $\frac{d\sigma_A^{WI}/dx}{d\sigma_{\rm CH}^{WI}/dx}$ ($A = {}^{12}$C, ^{56}Fe, ^{208}Pb) at $E = 7$ GeV and 25 GeV for the charged-current ν_l-A and $\bar{\nu}_l$-A DIS processes. The theoretical results are obtained in the kinematic region relevant for the MINERνA experiment ($W > 2$ GeV and $Q^2 > 1$ GeV^2) and are compared with the experimental data, as well as with the results obtained using the phenomenological models of Cloet *et al.* [8], Bodek-Yang [7], and GENIE Monte Carlo [6].

The results for the ratio $(\frac{d\sigma_A^{WI}/dx}{d\sigma_{\rm CH}^{WI}/dx})$ vs x in the case of ν_l-A scattering are presented in Fig. 14 and are summarized below:

(1) As the nuclear medium effects are approximately the same in carbon and CH, the ratio $\frac{d\sigma_{\rm C}^{WI}/dx}{d\sigma_{\rm CH}^{WI}/dx}$ (top panel) is expected to be close to unity. From the Fig. 14, one may notice that the deviation of the ratio from unity is small in $\frac{d\sigma_{\rm C}^{WI}/dx}{d\sigma_{\rm CH}^{WI}/dx}$; however, for $\frac{d\sigma_{\rm Fe}^{WI}/dx}{d\sigma_{\rm CH}^{WI}/dx}$ and $\frac{d\sigma_{\rm Pb}^{WI}/dx}{d\sigma_{\rm CH}^{WI}/dx}$ it becomes large, which shows the A dependence of the nuclear medium effects, especially the contribution of mesons, which increases with A at low and intermediate x. For example, at $E = 25$ GeV, the contribution of mesons is found to be 10% (7%) at $x = 0.1$, 2% (1%) at $x = 0.3$, and $< 1\%$ at $x = 0.6$ in lead (iron) when they are treated as isoscalar. It is important to notice that even for high-energy neutrino beams, the effect of the nuclear medium on the differential scattering cross section is significant.

(2) We have found that due to the mass dependence of nuclear medium effects, the difference between the results of $\frac{d\sigma_{\rm C}^{WI}/dx}{d\sigma_{\rm CH}^{WI}/dx}$ and $\frac{d\sigma_{\rm Fe}^{WI}/dx}{d\sigma_{\rm CH}^{WI}/dx}$ $(\frac{d\sigma_{\rm Pb}^{WI}/dx}{d\sigma_{\rm CH}^{WI}/dx})$ obtained by using the full model at $E = 25$ GeV (solid line) is ≃4% (7%) at $x = 0.05$, 6% (9%) at $x = 0.1$, and 3% (∼3%) at $x = 0.6$ when there is no constraint on the CoM energy W. While the cut of $W > 2$ GeV leads to a change of 1%–5% in this difference in the entire range of x, for example, there is further reduction of ≃2% at $x = 0.05$, 3% at $x = 0.1$, ≃5% at $x = 0.2$, and $< 1\%$ at $x = 0.6$ in the differential scattering cross section.

(3) To study the isoscalarity effect, we have obtained the results for $\frac{d\sigma_{\rm Fe}^{WI}/dx}{d\sigma_{\rm CH}^{WI}/dx}$ and $\frac{d\sigma_{\rm Pb}^{WI}/dx}{d\sigma_{\rm CH}^{WI}/dx}$ by treating iron and lead to be nonisoscalar (left panel) as well as isoscalar (right panel) targets (Fig. 14). The isoscalarity correction in asymmetric nucleus is found to be significant. For example, at $E = 25$ GeV, this effect is 2% (5%) and 5% (13%) at $x = 0.3$ and 0.7, respectively, in iron (lead) when no kinematical cut is applied on W.

(4) To observe the energy dependence of the scattering cross section, numerical results obtained using the full model with $Q^2 > 1$ GeV^2 and $W > 2$ GeV at $E = 25$ GeV (solid line with star) are compared with the corresponding results obtained at $E = 7$ GeV (double dash-dotted line). It may be observed that in the region of low and intermediate x, the results for $\frac{d\sigma_A^{WI}/dx}{d\sigma_{\rm CH}^{WI}/dx}$ at $E = 7$ GeV are smaller in magnitude from the results at $E = 25$ GeV, while with the increase in x, the ratio $\frac{d\sigma_A^{WI}/dx}{d\sigma_{\rm CH}^{WI}/dx}$ obtained for $E = 7$ GeV increases. Due to the energy dependence of the differential scattering cross section, the differences between the results obtained using the full model at the aforesaid energies, i.e., 7 GeV and 25 GeV, are ≃3% (5%), 2% (≃2%), and 12% (≃16%) at $x = 0.1$, $x = 0.3$ and $x = 0.75$, respectively, if iron (lead) is treated as an isoscalar nuclear target.

(5) Furthermore, we have compared our theoretical results with the corresponding experimental data of MINERνA, as well as with the different phenomenological models like that of Cloet *et al.* [8] (solid line with circle), Bodek *et al.* [7] (solid line with square), and GENIE MC [6] (solid line with triangle). It may be noticed that MINERνA's experimental data have large error bars due to statistical uncertainties, and the wide band around the simulation is due to the systematic error, which shows an uncertainty up to ∼20% [5]. Although the results of phenomenological models lie within this systematic error band, even then, none of the phenomenological models is able to describe the observed ratios in the whole region of x.

We have also made predictions for the $\bar{\nu}_l$-A scattering cross sections in the same kinematic region as considered in Fig. 14 corresponding to the MINERνA experiment and presented the results in Fig. 15, for the ratio $\frac{d\sigma_A^{WI}/dx}{d\sigma_{\rm CH}^{WI}/dx}$,

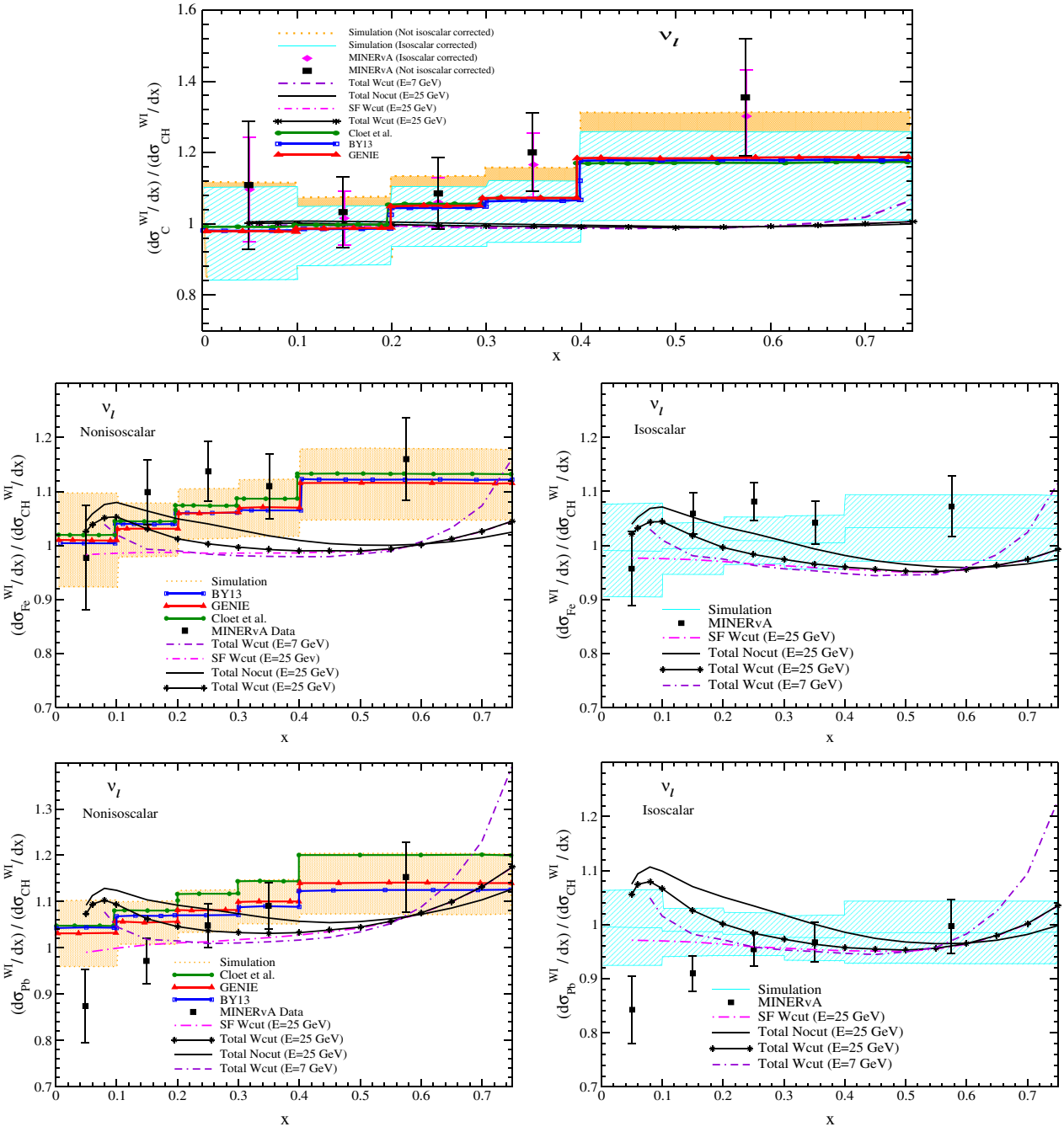

FIG. 14. $\frac{d\sigma_A^{WI}/dx}{d\sigma_{CH}^{WI}/dx}$ ($A = {}^{12}$C, ^{56}Fe, ^{208}Pb) vs x for incoming neutrino beams of energies $E = 7$ GeV and 25 GeV. The numerical results are obtained with the spectral function only (dash-dotted line: $E = 25$ GeV), as well as with the full model (solid line: $E = 25$ GeV, solid line with star: $E = 25$ GeV, double dash-dotted line: $E = 7$ GeV) at NNLO and are compared with the phenomenological results of Cloet *et al.* [8], Bodek-Yang [7], GENIE Monte Carlo [6], and with the simulated results [5]. The solid squares are the experimental points of MINERνA [5]. The results in the left and right panels are shown for the nonisoscalar and isoscalar nuclear targets, respectively.

($A = {}^{12}$C, ^{56}Fe, ^{208}Pb) vs x at $E = 7$ GeV and 25 GeV both without and with a cut of $W > 2$ GeV. The nuclear medium effects in $\frac{d\sigma_A^{WI}}{dx}$ for $\bar{\nu}_l$-A scattering are found to be qualitatively similar to ν_l-A scattering when no cut on CoM energy is applied; however, quantitatively they are different, especially at low and medium values of x. For example, at $E = 7$ GeV, the enhancement in the cross section when full calculations are applied from the results obtained using the spectral function is about 24% at $x = 0.25$ in ν_l-^{208}Pb scattering, while it is 65% in $\bar{\nu}_l$-^{208}Pb scattering, and the difference in the two results decreases with the increase in x. At $E = 25$ GeV, the enhancement in the cross section

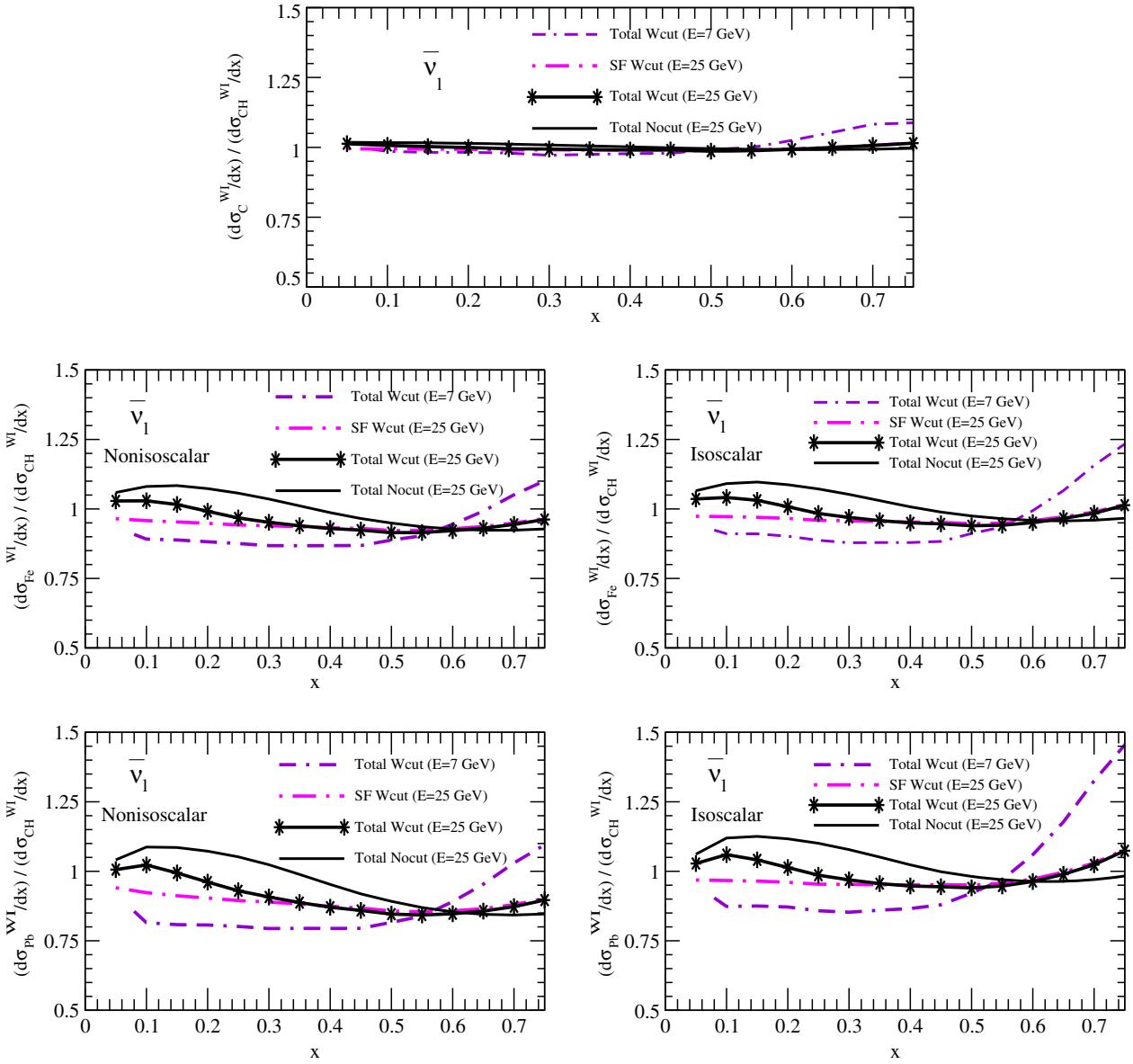

FIG. 15. $\frac{d\sigma_A^{WI}/dx}{d\sigma_{CH}^{WI}/dx}(A = {}^{12}\mathrm{C}, {}^{56}\mathrm{Fe}, {}^{208}\mathrm{Pb})$ vs x are shown for incoming antineutrino beam of energies $E = 7$ GeV and 25 GeV at NNLO. The numerical results are obtained using the spectral function only (dash-dotted line: $E = 25$ GeV) by applying a cut of $W > 2$ GeV and $Q^2 > 1$ GeV^2. The results using the full model are obtained with (solid line with star: $E = 25$ GeV and double dash-dotted line: $E = 7$ GeV) and without (solid line: $E = 25$ GeV) a cut of 2 GeV on the CoM energy but keeping $Q^2 > 1$ GeV^2. The results in the left and right panels are respectively shown for the nonisoscalar and isoscalar nuclear targets.

is about 20% at $x = 0.25$ in ν_l-^{208}Pb scattering, while it is ∼45% in $\bar{\nu}_l$-^{208}Pb scattering. When a cut of 2 GeV is applied on the CoM energy, then a suppression in the region of low and medium x is observed in the differential cross section, resulting in a lesser enhancement due to mesonic effects. For example, at $E = 25$ GeV, the enhancement due to the mesonic contributions becomes ∼18% (vs 20% without the cut) in ν_l-^{208}Pb scattering, while it is ∼28% (vs 45% without the cut) in $\bar{\nu}_l$-^{208}Pb scattering at $x = 0.25$. At $E = 7$ GeV, with a cut of 2 GeV on W, the enhancement is about 2% at $x = 0.25$ in ν_l-^{208}Pb scattering, while there is reduction in $\bar{\nu}_l$-A scattering, implying a small contribution from the mesonic part. This reduction in $\frac{d\sigma_A^{WI}}{dx}$ for $\bar{\nu}_l$-A scattering is about 15% in a wide region of x (≤ 0.6). When the results for $\frac{d\sigma_A^{WI}/dx}{d\sigma_{\mathrm{CH}}^{WI}/dx}$ using an antineutrino beam are compared with neutrino results, we find that without any cut on W, the results are similar, but with a cut for $E = 7$ GeV, there is enhancement at high x. This enhancement is larger in ^{208}Pb than in ^{56}Fe due to the large effect of Fermi motion in heavy nuclei.

IV. SUMMARY AND CONCLUSION

Our findings for the weak nucleon and nuclear structure functions and the differential scattering cross sections are as follows:

(1) The difference between the results of free nucleon structure functions $F_{iN}^{WI}(x, Q^2)$ $(i = 1, 2)$ evaluated at NLO with the HT effect and the results obtained at NNLO is almost negligible ($<1\%$). However, this difference is somewhat larger for $F_{3N}^{WI}(x, Q^2)$ at low x and low Q^2, which becomes smaller with an increase in Q^2. In the case of nucleons bound inside a nucleus, the HT corrections are further suppressed due to the presence of nuclear medium effects. Consequently, the results for $\nu_l/\bar{\nu}_l$-A DIS processes which are evaluated at NNLO have an almost negligible difference from the results obtained at NLO with the HT effect.

(2) The nuclear structure functions obtained with the spectral function only are suppressed from the free nucleon case in the entire region of x. By contrast, the inclusion of mesonic contributions results in an enhancement in the nuclear structure functions in the low and intermediate regions of x. Mesonic contributions are observed to be more pronounced with an increase in mass number, and they decrease with increasing x and Q^2. The results for the nuclear structure functions $F_{2A}^{WI}(x, Q^2)$ and $F_{3A}^{WI}(x, Q^2)$ with the full theoretical model show good agreement with the experimental data of CCFR [72], CDHSW [73], NuTeV [74], and CHORUS [75], especially at high x and high Q^2. Predictions are also made for ^{40}Ar that may be useful in analyzing the experimental results of DUNE [2,3] and ArgoNeuT [4].

(3) We have found nuclear medium effects to be different in electromagnetic and weak interaction channels, especially for the nonisoscalar nuclear targets. The contribution of strange and charm quarks is found to be different for the electromagnetic- and weak-interaction-induced processes off a free nucleon target, which also gets modified differently for the heavy nuclear targets. Furthermore, we have observed that the isoscalarity corrections, significant even at high Q^2, are not the same in $F_{1A}^{WI}(x, Q^2)$ and $F_{2A}^{WI}(x, Q^2)$.

(4) The nuclear medium effects are found to be important in the evaluation of differential scattering cross sections. We have observed that in the $\bar{\nu}_l$-A reaction channel, the nuclear medium effects are more pronounced than in the case of the ν_l-A scattering process. Our results of $\frac{1}{E}\frac{d^2\sigma_A^{WI}}{dxdy}$, $(A = {}^{56}\mathrm{Fe}, {}^{208}\mathrm{Pb})$ obtained using the full model show a reasonable agreement with the experimental data of NuTeV [74] and CHORUS [75] for the neutrino- and antineutrino-induced DIS processes. Theoretical results of the differential cross section are also found to be in good agreement with the phenomenological results of nCTEQnu nuclear PDF parametrizations [77] in the intermediate as well as the high regions of x for all values of y.

(5) The present theoretical results for the ratio $\frac{d\sigma_A^{WI}/dx}{d\sigma_{\mathrm{CH}}^{WI}/dx}$, $(A = {}^{12}\mathrm{C}, {}^{56}\mathrm{Fe}, {}^{208}\mathrm{Pb})$, when compared with the different phenomenological models and MINERνA's experimental data on ν_l-A scattering, imply that a better understanding of nuclear medium effects is required in the $\nu_l(\bar{\nu}_l)$-nucleus deep inelastic scattering. We have also made predictions for the $\bar{\nu}_l$-A DIS cross sections relevant for the upcoming MINERνA results.

To conclude, the present theoretical results provide information about the energy dependence, the effect of the CoM energy cut, medium modifications, and isoscalarity correction effects on the nuclear structure functions and cross sections for the deep inelastic scattering of (anti)neutrinos from various nuclei. This study will be helpful to understand the present and future experimental results from MINERνA [5], ArgoNeuT [4], and DUNE [2,3] experiments.

ACKNOWLEDGMENTS

F. Zaidi is thankful to the Council of Scientific & Industrial Research (CSIR), India, for providing the research associate fellowship with Grant No. 09/112 (0622)2K19 EMR-I. M. S. A. and S. K. S. are thankful to the Department of Science and Technology (DST), Government of India, for providing financial assistance under Grant No. EMR/2016/002285. I. R. S. acknowledges support from the Spanish Ministerio de Economia y Competitividad under Grant No. FIS2017-85053-C2-1-P, and by Junta de Andalucia (Grant No. FQM-225).

[1] F. Zaidi, H. Haider, M. Sajjad Athar, S. K. Singh, and I. Ruiz Simo, Phys. Rev. D **99**, 093011 (2019).
[2] B. Abi *et al.* (DUNE Collaboration), arXiv:1807.10327.
[3] R. Acciarri *et al.* (DUNE Collaboration), arXiv:1512.06148.
[4] R. Acciarri *et al.* (ArgoNeuT Collaboration), Phys. Rev. D **89**, 112003 (2014).
[5] J. Mousseau *et al.* (MINERνA Collaboration), Phys. Rev. D **93**, 071101 (2016).

[6] C. Andreopoulos *et al.*, Nucl. Instrum. Methods Phys. Res., Sect. A **614**, 87 (2010).
[7] A. Bodek and U. K. Yang, arXiv:1011.6592; Nucl. Phys. B, Proc. Suppl. **112**, 70 (2002).
[8] I. C. Cloet, W. Bentz, and A. W. Thomas, Phys. Lett. B **642**, 210 (2006).
[9] C. G. Callan, Jr. and D. J. Gross, Phys. Rev. Lett. **22**, 156 (1969).
[10] M. Hirai, S. Kumano, and T.-H. Nagai, Phys. Rev. C **76**, 065207 (2007).
[11] K. J. Eskola, H. Paukkunen, and C. A. Salgado, J. High Energy Phys. 04 (2009) 065.
[12] D. de Florian, R. Sassot, P. Zurita, and M. Stratmann, Phys. Rev. D **85**, 074028 (2012).
[13] K. Kovarik *et al.*, Phys. Rev. D **93**, 085037 (2016).
[14] K. Kovarik *et al.*, Few Body Syst. **52**, 271 (2012).
[15] N. Kalantarians, C. Keppel, and M. E. Christy, Phys. Rev. C **96**, 032201 (2017).
[16] S. V. Akulinichev *et al.*, Phys. Lett. **158B**, 485 (1985); Phys. Rev. Lett. **55**, 2239 (1985); Phys. Lett. B **234**, 170 (1990).
[17] G. V. Dunne and A. W. Thomas, Phys. Rev. D **33**, 2061 (1986).
[18] R. P. Bickerstaff and A. W. Thomas, J. Phys. G **15**, 1523 (1989).
[19] C. Ciofi Degli Atti and S. Liuti, Phys. Lett. B **225**, 215 (1989).
[20] S. A. Kulagin, Nucl. Phys. **A500**, 653 (1989).
[21] M. Arneodo, Phys. Rep. **240**, 301 (1994).
[22] O. Hen, D. W. Higinbotham, G. A. Miller, E. Piasetzky, and L. B. Weinstein, Int. J. Mod. Phys. E **22**, 1330017 (2013).
[23] G. Piller and W. Weise, Phys. Rep. **330**, 1 (2000).
[24] E. Marco *et al.*, Nucl. Phys. **A611**, 484 (1996).
[25] O. Benhar, V. R. Pandharipande, and I. Sick, Phys. Lett. B **469**, 19 (1999); **410**, 79 (1997).
[26] J. R. Smith and G. A. Miller, Phys. Rev. Lett. **91**, 212301 (2003); **98**, 099902(E) (2007).
[27] S. A. Kulagin and R. Petti, Nucl. Phys. **A765**, 126 (2006).
[28] C. Ciofi degli Atti, L. L. Frankfurt, L. P. Kaptari, and M. I. Strikman, Phys. Rev. C **76**, 055206 (2007).
[29] S. A. Kulagin and R. Petti, Phys. Rev. D **76**, 094023 (2007).
[30] M. Sajjad Athar, S. K. Singh, and M. J. Vicente Vacas, Phys. Lett. B **668**, 133 (2008).
[31] M. Sajjad Athar, I. Ruiz Simó, and M. J. Vicente Vacas, Nucl. Phys. **A857**, 29 (2011).
[32] H. Haider, I. Ruiz Simo, M. Sajjad Athar, and M. J. Vicente Vacas, Phys. Rev. C **84**, 054610 (2011).
[33] L. Frankfurt and M. Strikman, Int. J. Mod. Phys. E **21**, 1230002 (2012).
[34] H. Haider, I. Ruiz Simo, and M. Sajjad Athar, Phys. Rev. C **85**, 055201 (2012).
[35] H. Haider, I. Ruiz Simo, and M. Sajjad Athar, Phys. Rev. C **87**, 035502 (2013).
[36] H. Haider, M. Sajjad Athar, S. K. Singh, and I. Ruiz Simo, Nucl. Phys. **A940**, 138 (2015).
[37] S. Malace, D. Gaskell, D. W. Higinbotham, and I. C. Cloët, Int. J. Mod. Phys. E **23**, 1430013 (2014).
[38] M. Ericson and A. W. Thomas, Phys. Lett. **128B**, 112 (1983).
[39] R. P. Bickerstaff and G. A. Miller, Phys. Lett. **168B**, 409 (1986).
[40] E. L. Berger and F. Coester, Annu. Rev. Nucl. Part. Sci. **37**, 463 (1987).
[41] R. L. Jaffe, Phys. Rev. Lett. **50**, 228 (1983).
[42] H. Mineo, W. Bentz, N. Ishii, A. W. Thomas, and K. Yazaki, Nucl. Phys. **A735**, 482 (2004).
[43] I. C. Cloet, W. Bentz, and A. W. Thomas, Phys. Rev. Lett. **95**, 052302 (2005).
[44] O. Nachtmann and H. J. Pirner, Z. Phys. C **21**, 277 (1984).
[45] F. E. Close, R. G. Roberts, and G. G. Ross, Phys. Lett. **129B**, 346 (1983).
[46] L. L. Frankfurt and M. I. Strikman, Phys. Rep. **160**, 235 (1988).
[47] N. Armesto, J. Phys. G **32**, R367 (2006).
[48] D. F. Geesaman, K. Saito, and A. W. Thomas, Annu. Rev. Nucl. Part. Sci. **45**, 337 (1995).
[49] H. Haider, F. Zaidi, M. Sajjad Athar, S. K. Singh, and I. Ruiz Simo, Nucl. Phys. **A943**, 58 (2015).
[50] S. A. Kulagin and R. Petti, Phys. Rev. C **82**, 054614 (2010).
[51] H. Haider, M. Sajjad Athar, S. K. Singh, and I. R. Simo, J. Phys. G **44**, 045111 (2017).
[52] H. Haider, F. Zaidi, M. Sajjad Athar, S. K. Singh, and I. Ruiz Simo, Nucl. Phys. **A955**, 58 (2016).
[53] L. A. Harland-Lang, A. D. Martin, P. Motylinski, and R. S. Thorne, Eur. Phys. J. C **75**, 204 (2015).
[54] J. A. M. Vermaseren, A. Vogt, and S. Moch, Nucl. Phys. **B724**, 3 (2005).
[55] S. Moch, J. A. M. Vermaseren, and A. Vogt, Phys. Lett. B **606**, 123 (2005).
[56] S. Moch, J. A. M. Vermaseren, and A. Vogt, Nucl. Phys. **B813**, 220 (2009).
[57] M. Dasgupta and B. R. Webber, Phys. Lett. B **382**, 273 (1996).
[58] I. Schienbein *et al.*, J. Phys. G **35**, 053101 (2008).
[59] P. Fernandez de Cordoba and E. Oset, Phys. Rev. C **46**, 1697 (1992).
[60] W. L. van Neerven and A. Vogt, Nucl. Phys. **B568**, 263 (2000); **B588**, 345 (2000).
[61] K. G. Wilson, Phys. Rev. **179**, 1499 (1969).
[62] E. V. Shuryak and A. I. Vainshtein, Nucl. Phys. **B199**, 451 (1982).
[63] G. Altarelli and G. Parisi, Nucl. Phys. **B126**, 298 (1977); V. N. Gribov and L. N. Lipatov, Yad. Fiz. **15**, 781 (1972) [Sov. J. Nucl. Phys. **15**, 438 (1972)]; L. N. Lipatov, Yad. Fiz. **20**, 181 (1974) [Sov. J. Nucl. Phys. **20**, 94 (1975)]; Y. L. Dokshitzer, Zh. Eksp. Teor. Fiz. **73**, 1216 (1977) [Sov. Phys. JETP **46**, 641 (1977)].
[64] C. Garcia-Recio, J. Nieves, and E. Oset, Nucl. Phys. **A547**, 473 (1992).
[65] H. De Vries, C. W. De Jager, and C. De Vries, At. Data Nucl. Data Tables **36**, 495 (1987).
[66] G. Baym and G. E. Brown, Nucl. Phys. **A247**, 395 (1975).
[67] A. D. Martin, R. G. Roberts, W. J. Stirling, and R. S. Thorne, Eur. Phys. J. C **4**, 463 (1998).
[68] K. Wijesooriya, P. E. Reimer, and R. J. Holt, Phys. Rev. C **72**, 065203 (2005).

[69] P. J. Sutton, A. D. Martin, R. G. Roberts, and W. J. Stirling, Phys. Rev. D **45**, 2349 (1992).
[70] M. Gluck, E. Reya, and A. Vogt, Z. Phys. C **53**, 651 (1992).
[71] B. Z. Kopeliovich, J. G. Morfin, and I. Schmidt, Prog. Part. Nucl. Phys. **68**, 314 (2013).
[72] E. Oltman *et al.*, Z. Phys. C **53**, 51 (1992).
[73] J. P. Berge *et al.*, Z. Phys. C **49**, 187 (1991).
[74] M. Tzanov *et al.* (NuTeV Collaboration), Phys. Rev. D **74**, 012008 (2006).
[75] G. Onengut *et al.* (CHORUS Collaboration), Phys. Lett. B **632**, 65 (2006).
[76] J. G. Morfin, J. Nieves, and J. T. Sobczyk, Adv. High Energy Phys. **2012**, 934597 (2012).
[77] J. G. Morfin (private communication).